Field Emission Cathodes Based on Structured Carbon Nanotube Arrays

Z. Cheng[1], L. Sun[1], Z. Y. Li[2], P. Serbun[3], N. Kargin[4], V. Labunov[5*], B. Shulitski[5], I. Kashko[5], D.Grapov[5], G.Gorokh[5]

Abstract— **Field emission properties of the structured carbon nanotube cathodes were investigated by field emission scanning microscopy, scanning electron microscopy and integral field emission measurements with luminescence screen. The carbon nanotube arrays were synthesized by the atmospheric pressure floating catalyst chemical vapour deposition method under the high temperature pyrolysis of ferrocene/xylene solution. Varying arrays of carbon nanotube columns and blocks were fabricated on Si, SiO$_2$ and porous anodic alumina substrates. Well-aligned field emission from nearly 100% of the patches at electric field <10 V/µm in direct current and pulsed mode integrally and locally was observed. High current capabilities up to mA currents for structured carbon nanotube cathodes were achieved. Integral field emission measurements with luminescence screen and processing under N$_2$ and O$_2$ exposures of up to 3×10^{-5} mbar demonstrated homogeneous current distribution and long-term stability of the structured carbon nanotube cathodes.**

Index Terms— **carbon nanotubes, field emission catchodes, structured carbon nanotube arrays, field emission scanning microscope.**

I. INTRODUCTION

Since the discovery of carbon nanotubes (CNTs) by Iijima in 1991, continuous research of them reveals more and more unique properties and new areas of application [1]. One of the promising and intensively studied fields of application is CNT-based field-emission cathodes (FECs). FECs can be used in a series of devices, such as high brightness flat-panel displays [2], compact X-ray sources [3-7], powerful microwave amplifiers [8-10]; high-performance luminescent lamps [11, 12]; compact high-frequency electron sources, sources of synchrotron radiation [13], vacuum sensors [14] etc. The attractiveness of CNTs for these applications is due

Z.Cheng[1], Institute of Electron Device & Application, Hangzhou Dianzi University, Hangzhou, China.
L.Sun[1], Institute of Electron Device & Application, Hangzhou Dianzi University, Hangzhou, China.
Z.Y.Li[2], North-China Electromagnetic Protection Research Institute, Taiyuan, China.
P. Serbun[3], Bergische Universität Wuppertal, Wuppertal, Germany.
N. Kargin[4], National Research Nuclear University MEPhI, Moscow, Russia.
V.Labunov[5*], Belarusian State University of Informatics and Radioelectronics, Minsk, Belarus
B.Shulitski[5], Belarusian State University of Informatics and Radioelectronics, Minsk, Belarus.
I. Kashko[5], Belarusian State University of Informatics and Radioelectronics, Minsk, Belarus.
D. Grapov[5], Belarusian State University of Informatics and Radioelectronics, Minsk, Belarus.
G.Gorokh[5], Belarusian State University of Informatics and Radioelectronics, Minsk, Belarus.

to their electrical, chemical, thermal and mechanical properties. Advantageous for FECs high electrical conductivity and emissivity are reached owing to quasi one-dimensional structure and naturally high aspect ratio of CNTs [15]. Regardless of the field of FECs application, a number of requirements to their characteristics must be satisfied. Among them are the high emission efficiency; low threshold and operating voltages; high homogeneity, density and stability of electron emission. Moreover, FECs should have a firm construction providing a good electrical contact and adhesion of CNTs to the cathode electrode, which, in turn, must allow electrical connection to the bonding pads and metal interconnections, and it should be compatible with the technology of microelectronics.

Carbon nanotubes mostly satisfy the requirements mentioned above [16]. The extent of their meet of these requirements depends on the FECs construction.

Mechanism of the Field emission

The basic parameter characterizing efficiency of FECs is emission current density, J, which is described by the modified Fauler-Nordheim (FN) equation [17-19]:

$$J = \frac{AS\beta^2 E^2}{\phi} \exp\left[\frac{-B\phi^{3/2}}{\beta E}\right] \qquad (1)$$

where E is the external electric field, V/cm, φ is the work function of electrons, eV, is the field extension factor, S is the parameter which can be interpreted as the area of emission, A=154 and B=6830 are constants. For multi-wall CNTs, φ =5 eV [20, 21].

Experimentally, and S can be found from the slope of FN plot which represents the dependence ln(I/E2) = f(1/E), and for the case of field-emission is the straight line. The required parameters can be estimated as

$$\beta = \frac{B\phi^2}{K} \quad S = \frac{\phi}{A\beta^2 \exp(C)} \qquad (2)$$

where K = d(ln(I/E2))/d(1/E) is the slope of the line, C is the intersection of the FN curve and Y-axis.

The field extension factor, β, defines the degree of conversion of external macroscopic field into the local microscopic one at the tip of CNT, which is responsible for the electron emission. Threshold voltage, i.e. the voltage value at which the electron emission starts, is inversely proportional to the field extension factor.

In ref. [19] the idea of hybrid scheme of field extension is

put forward, according to which the field extension has two constituents: the field extension factor, β (internal one), and γ factor (external one) which is defined by the electrostatic screening effect caused by neighboring CNTs.

The internal factor β can be determined when electric field is concentrated around a single free-standing CNT. It depends on the geometrical parameters of CNT, and is calculated as β=l/r [22-25], where l is the length of CNT, r is the radius of the curvature of the CNT tip which can have various shapes (H-like, flat or sharp) [26]. The radius of the CNT tip curvature is equal to the radius of CNT in the case of a closed-tip CNT, and is much smaller than the CNT's radius in the case of an open-tip CNT. The external factor can be calculated by numerical computing.

In practice, the external factor is the most critical parameter affecting the field current density of FEC [24-26]. It was shown, that the optimal emission efficiency is reached when the length of CNT, L, at least ten times exceeds its diameter, d, and the distance between neighboring CNTs, H, is equal 2L, i.e. H=2L=2•10d=20d [27]. This means that a CNT array must be quite sparse. On the other hand, the CNT array shouldn't be too thin, since it would lead to the decrease of the emission current density. Therefore, for the high-efficiency FEC the optimal length, diameter and density of CNTs are required

II. CNT-BASED FECs CONSTRUCTIONS AND METHODS OF ITS PRODUCTION

The CNT-based FECs of any construction are composed of the passive element, i.e. dielectric or conductive substrate, and active element, such as CNT array, emitting electrons located on the surface of the substrate.

Depending on the electronic assembly into which FECs are integrated, there might be two types of FECs, when the CNT array's active element is located either on a dielectric substrate (in order to be isolated from the integrated circuit), or on a conductive substrate (like silicon, the material of the integrated circuit).

CNT-based FECs can be made using various approaches. The simplest one is screen printing of CNTs-containing epoxy composites with subsequent annealing [28-32]. This method can be applied for producing large-area flat panel displays. The drawback of the present technology is that CNTs protrude from the epoxy not uniformly which causes the nonuniformity and instability of electron emission. To avoid this, current treatment of composite at high voltages is carried out what leads to destruction of the "strongest" emitting sites, though it will result in higher operating voltages of FEC.

Another method consists in formation of arrays of vertically aligned CNTs by chemical vapor deposition (CVD) at various substrates. However, for such FECs the optimal emission efficiency conditions can not be reached, since H~d in this case [16]. Thus, in order to use such CNT arrays as field emitters, their structuring is required. Structured CNT arrays are usually obtained by growing CNTs on the pre-patterned on the substrate catalyst film ("localized catalyst CVD") [33-36]. Sometimes, additionally or independently, floating catalyst formed by metallocene

decomposition ("floating catalyst CVD") is used for CNT arrays synthesis [37]. In the last case, the CNT array structuring obtained at the conditions of so-called "selective growth" when nanotubes are formed only on a desired type of surface.

Structured CNT arrays composing FEC may have various configurations, for example, pillars of roundish or rectangular cross-section [15].

In case if the diameter of the CNT pillar exceeds the cathode-to-anode distance, the electrical field applied to such CNT cathode will be much larger at the edges of the pillars as compared to their middle areas, even not taking into account the screening effects. Thus, the strongest emission sites are at the edges of the CNT pillars where the screening effect is less pronounced. Therefore, there might be a case when majority of the emitters in the middle of the cathode will be not active. In order to avoid this effect, it is necessary to decrease the diameter of CNT pillars, as well as the parameters corresponding to optimal emission conditions. The drawback of CNT-based cathodes obtained by thermal floating catalyst CVD is weak adhesion of CNTs to the silicon substrate. Hence, the improved technological process is needed to improve mechanical contact of CNTs to cathode electrode.

The third approach for CNT-based cathode fabrication is the use of porous anodic aluminum oxide (AAO) as a matrix for CNT growth. The pore diameter and inter-pore distance can be controlled by anodizing regimes and/or pore expansion [38]. CNTs synthesis is going on with the use of metal catalysts [39-41] ore without [42, 43]. In the first case, regardless whether catalyst particles are localized at the pores walls or at their bottoms, CNTs are growing from these particles and AAO has no effect on their structure, and it is difficult to control CNT diameters and lengths. If CNTs are being synthesized without catalysts or with the use of floating catalyst, at the pores walls the graphitic tubular structures are formed which geometry corresponds to the AAO pores [44]. These graphitic tubules have a good adhesion both to the AAO and to the substrate, which makes this type of CNT-based cathode most stable and firm from the point of the construction and production/operation processes. However, it also has some limitations, such as, for example, high threshold voltage, since the pores are not distant enough (around 100 nm) and the screening effect predominates. Moreover, the graphitic tubules formed inside them have quite big diameters and thick walls (tens of nanometers) creating obtuse emission edges. The tubules walls have flaky graphitic structure with plenty of defects in crystal structure [45]. The flakes edges most probably represent "weak points" where the layers can be pilled during emission process. Thereby, emission properties of graphitic tubules worse than that of traditional CNTs. Evidently, one of the ways to improve the emission properties of CNT/AAO cathodes is their structuring.

A number of constructions of the Field Emission Cathodes (FECs) on the basis of CNT arrays have been constructed and tested. In order to avoid the shielding effect created by closely allocated CNTs in the array a special technology of CNT arrays structuring has been developed. The structuring was realized by the CNTs selective growth on the

metal/semiconductor/dielectric surfaces. Three particular constructions of FECs are investigated: CNT FEC on a dielectric substrate, CNT FEC on a conductive substrate, CNT in AAO FEC on a conductive substrate.

III. MEASUREMENTS OF THE CNT-BASED FECs PARAMETERS

A. FE Scanning Microscope (FESM)

The FESM (Figure 1) is an advanced microscope for investigation of FE site distributions on "flat" cathodes of up to 25 x 25 mm2. The cathode is xy-surface tilt-corrected with respect to the anode to achieve a constant gap Δz within ±5 µm for the full scan area. The measurements are done in ultrahigh vacuum (UHV) of 10^{-9} mbar by means of LabView-automated non-destructive regulated voltage scans V(x, y) at a fixed FE current (typ. 1 nA). It employs a PID-regulated power supply FUG HCN100M-10000 [46] controlled by the FE current as measured with a digital picoammeter Keithley 6485 or an analog electrometer Keithley 610C [47] as described elsewhere [48, 49].
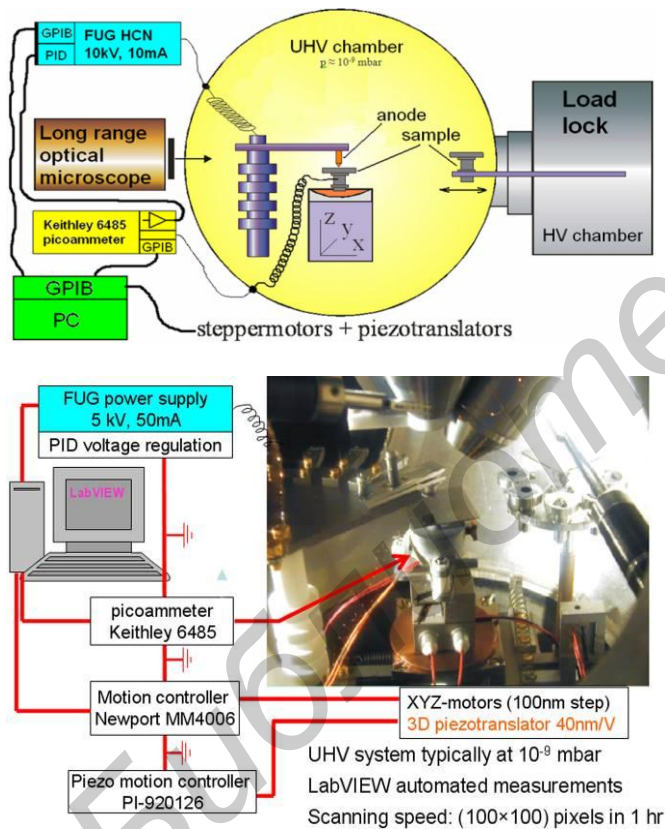

Figure 1: Schematic illustration (top) and inner view (bottom) of the FESM [48].

The power supply provides up to 10 mA current and 10 kV voltages, which corresponds up to 500 MV/m macroscopic field at 20 µm gap. By in-situ exchange between needle-anodes and truncated cone anodes, the emitter distribution, homogeneity, and efficiency of FE from selected cathode areas can be verified with the required resolution and the integral current of arbitrarily chosen individual emitters or patches can be measured. The needle anodes have a tip apex radius of Ra ≥ 1 µm, while the truncated cone anodes are up to 300 µm in diameter. The anodes are mechanically prepared and finally smoothed or, in case of the needle-anodes, sharpened by means of electrochemical etching in 10% water solution of NaOH and consist of tungsten-tantalum alloy 90:10.

Each FE investigation is done by means of the voltage scans following by the local investigations of selected patches. The onset field Eon as well as an effective field enhancement factor βeff, emitting area S, and the maximum current capability Imax of arbitrarily or systematically chosen from the voltage maps emitters can be measured as well. The last two parameters are calculated from the measured I-V characteristics of the emitters using the modified Fowler-Nordheim (FN) law [50] for field emission.

Nordheim functions, which depends on the relative reduction of the barrier through the image charge. For simplicity, the image charge correction is ignored and both parameters are set to 1.

The macroscopic electric field E is calibrated for each emitter as the linear slope of the PID-regulated V(z) dependence for 1 nA current. Moreover, the real distance d between the tip anode and the relevant emitter is determined by the linear extrapolation of each V(z) curve to zero voltage (Figure 2, [51]).
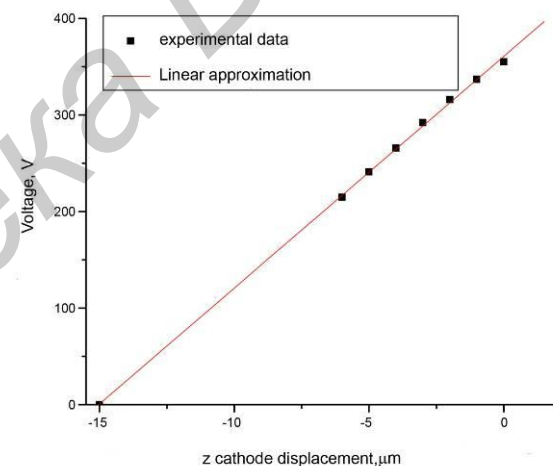

Figure 2: Determination of real distance d between the anode and e relevant emitter [48].

For *d* values close to or smaller than the mean height *h* of a nanostructure, the effective field enhancement factor β_{eff} is not only given by the intrinsic field enhancement of the nanostructure, but is also influenced by the geometric field enhancement β_{an} provided by the nearby anode as shown in the Figure 3.
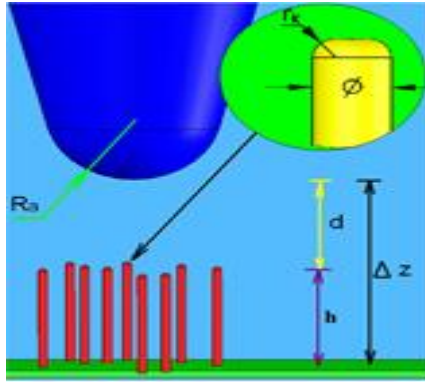
Figure 3: Schematic of the measurement geometry of nanostructures with a needle anode defining all important parameters [48].

The reduction of β_{eff} with d was confirmed experimentally for a single CNT [52] and can be estimated based on a two-region FE model of Zhong et al [53] as

$$1/\beta_{eff} \sim 1/\beta_{ns} + 1/\beta_{an} = r_k/h + r_k/d \qquad (3)$$

This model is not exact for patches of nanostructures yet because of influences of mutual shielding and field reduction α due to the anodes geometry [23] on β_{eff} have to be taken into account, too. The decrease of the field enhancement factor at decreased distance d has been well confirmed experimentally by measurements on randomly distributed Au-NW [54]. Therefore, the effect is very important for correct design of triode structures of real applications.

B. Integral Measurement System with Luminescent Screen (IMLS)

The IMLS is used for determination of the integral current of the cathodes in dc and pulsed modes up to 5kV voltage (17 V/µm field at 300 µm gap) and 50mA current (Figure 4). Serial resistors used for the cathode protection against discharges and fast current readout. A resistive voltage divider is used for the high voltage readout. Registration of current and voltage signals is done by a PC equipped with a LabView software and an analog to digital (ADC) converter (Keithley KPCI-3102 [47]) after a unity gain (current) amplification of the signals. The ammeter (Keithley 2000 multimeter in ammeter mode) is used for the current calibration and dc measurements (via GPIB interface).
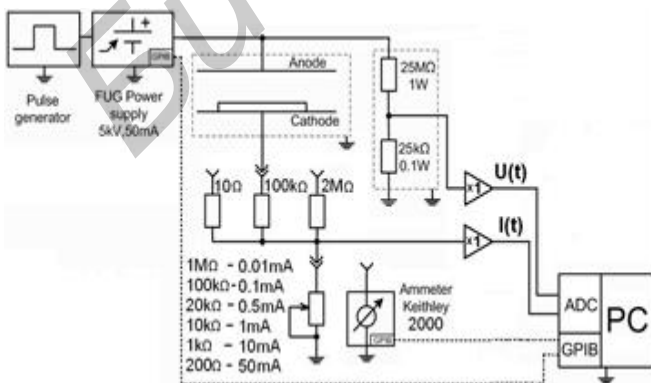

Figure 4: Block diagram of the electric circuit of the IMLS in diode configuration [48].

For the pulsed measurements, however, it is not suitable because of its limited speed. The IMLS was correspondingly equipped with a data acquisition system based on a self-developed software using LabView programming package. It allows registration of full signals of the current and voltage in the dc and pulsed modes as well as their time dependence during the long-term tests. The system can be switched from the diode to a triode configuration as shown in the Figure 5.

The FE current distribution from the cathodes shown by the luminescent screen is stored with a CCD camera Nikon Coolpix 950 [55] or Basler acA1300-30 [56] with zoom-objective providing around 20 µm lateral resolution (limited by grain size of luminescent layer). The image signal from the Nikon camera is transmitted to a PC via a frame grabber Matrox Meteor II [57] whereas the images from the Basler one is directly stored as time- and I-V-referenced data by the LabView package via TCP/IP interface. Finally the images can be additionally processed with an image analyzing software AnalySIS FIVE® [58].

The long-term performance of the cathodes can be tested in the dc mode at a base pressure of about 10^{-7} mbar as well as under enhanced nitrogen or oxygen pressure levels up to 10^{-5} mbar provided by filtered high-purity gases (99,995%) through a needle valve for up to 5 hours. A quadrupole mass spectrometer (QMG-112) served both for partial pressure measurements and control of a luminescence layer evaporation with a sensitivity limit of 5×10^{-11} mbar (e.g. for S).
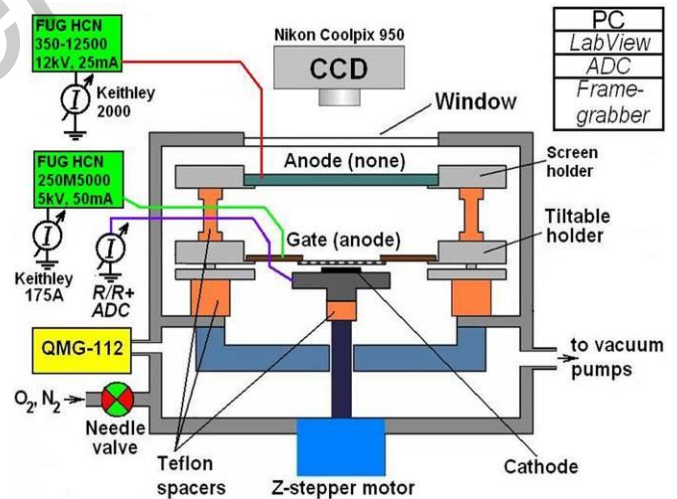

Figure 5: Triode (diode) configurations of the IMLS [48].

C. Measurements of the Field Emission characteristics of the CNT-based cathodes

The Field Emission (FE) properties of the structured CNT cathodes were investigated with two instruments, i.e. the field emission scanning microscope (FESM) for spatially resolved measurements and the integral current diode configuration with luminescent screen (IMLS) for applicational issues [49]. After tilt correction of the xy-surface within ±1 µm, the LabView-automated FESM with a Ø30 µm anode and a PID-regulated voltage supply (FUG HCN250M5000) controlled by the FE current (digital Keithley 6485) was used

for the non-destructive imaging of the potential emitter distribution over the whole structured cathode [59]. In addition, local measurements on selected pillars were made with needle anodes (tip radius 8 µm or 3 µm). The macroscopic electric field E was calibrated for each FE site as linear slope of the V(z)-dependence for 1 nA current, the linear extrapolation of which also reveals the real distance between the tip and the relevant emitter [51]. The integral current of the structured CNT cathodes was determined in dc and pulsed modes up to 5 kV voltage and 50 mA current by means of the IMLS equipped with a data acquisition system on the basis of LabView. Serial resistors were used for the cathode protection against discharges and fast current readout via an ADC converter (KPCI-3102). The current distribution shown by the IMLS images with 20 µm lateral resolution were stored with a CCD camera (Nikon Coolpix 950) and a frame grabber (Matrox Meteor II) and processed with image analysis software ANALYSIS® [60]. Finally, the long-term performance of the CNT cathodes was tested in the IMLS dc mode at a base pressure of about 2×10^{-7} mbar as well as under enhanced nitrogen or oxygen pressure levels up to 3×10^{-5} mbar provided by filtered high-purity gases (99,995%) through a needle valve for some hours. A quadrupole mass spectrometer (QMG-112) served both for partial pressure measurements and control of luminescence layer evaporation with a sensitivity limit of 5×10^{-11} mbar (e.g. for S).

IV. THE CNT FEC ON DIELECTRIC SUBSTRATE

A. The construction and the production technology of CNT FEC on dielectric substrate

The developed construction of the CNT FEC on a dielectric substrate is composed of a passive element: Si/SiO$_2$ substrate with planar Ti Inter Digitated Electrodes (IDEs), and an active element: a meander shape structured CNT array in the inter electrodes space and continuous array of CNTs around Ti electrodes, selectively grown on SiO$_2$ surface [60, 61].

The construction of the passive element of CNT FEC on the dielectric substrate is presented in Figure 6.

Si/SiO$_2$ structure with the thermally grown SiO$_2$ layer was chosen as a substrate. On the top of SiO2 the planar titanium IDEs were formed by the microelectronics technology. Ti was chosen as a material of the electrodes for two reasons. First, it is a high-melting material which is crucial for the high-temperature CNTs synthesis process (up to 900°C). Secondly, as it is shown by a number of investigations, the Ti film suppresses the CNT growth completely on its surface resulting in the strong selectivity of CNTs growth on SiO2 [60]. The Inter Digitated shape of Ti electrodes was chosen because they have the meander shape spacing between them, in which the meander shape CNT array would be synthesized, which has very long line of edges for the efficient electron field emission.

As it is seen from Figure 6a, the IDEs have the meander shape spacing between them. The area of IDEs is 350µm×440µm. The size of the meander area is 180×350 µm. The fingers of IDEs have dimensions of 13,5 µm in width and 180 µm in length. The distance between fingers is 3,85 µm. IDEs (49 pcs.) are allocated at the Si/SiO2 chip with the dimensions of 5mm ×5mm (Figure 6b).

The technology of selective growth of the arrays of vertically aligned CNTs synthesized on SiO$_2$ surface of SiO$_2$/Ti topology is described in refs. [60, 61].

Briefly, CNT arrays were synthesized by the atmospheric pressure CVD method by means of a high temperature pyrolysis of ferrocene/xylene (feeding) solution at atmospheric pressure. N$_2$ was used as a gas-carrier. The feeding solution was delivered into the synthesis zone by the dosed injection. The advantages of the injection process are that it enables variation of the type of hydrocarbon, percentage content of catalyst in the solution, does not require the additional step of annealing in order to obtain highly uniform distribution of catalyst nanoparticles on the substrate surface, and is compatible with the microelectronics technology. The synthesis process was realized in the tubular type quartz reactor of the specially constructed equipment [62].

A lot of investigations have been done to find optimal regimes of selective growth of CNT arrays on the surface of SiO$_2$/Ti topology [63]. The CNT synthesis process is influenced, first of all, by the number of the gas-dynamical parameters, such as the rate of injection of the feeding solution into the reaction zone, v, and the rate of gas-carrier flow V_{N_2}, the concentration of catalyst source in the feeding solution, n, temperature, T, and duration of the synthesis process, t.
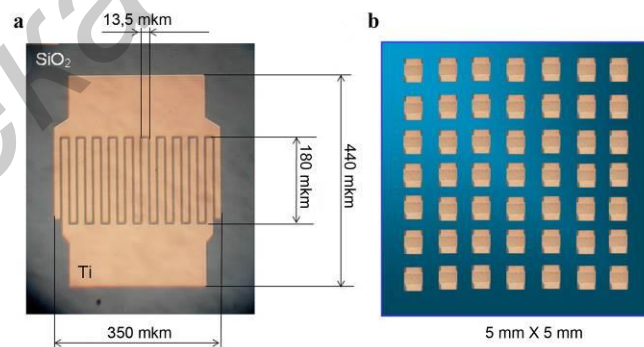

Figure 6: Top view of FEC's passive element composed of Si/SiO$_2$ substrate with planar Ti IDEs on top: (a) construction of a single passive element (optical microscopy), (b) schematic view of the Si/SiO$_2$ chip with 49 pieces of Ti IDEs.

A systematic multifactor experiment has been carried out what made it possible to determine the conditions of the selective growth of CNT arrays on SiO$_2$ and Ti surfaces of Ti/SiO$_2$ topology [64]. The following values of the parameters were chosen:

v=1 см3 min-1, =100 см3•min-1 (permanent parameters); n=0,5%, 1%, 5%, 10%; T=1050 K, 1100 K, 1150 K (variable parameters). The most distinctive selectivity and well defined geometry were obtained at T=1150 K and 1) n=10%, t=0,5 min (Figure 7a,b,e); 2) n=5%, t=1 min (Figure 7c,d).

In Figure 7 one can observe a single FEC, containing bulk CNT array (1), Ti electrodes (2) and CNT meander (3) (Figure 7a); matrix of FECs (Figure 7b); different height of the bulk CNT array and CNT meander (Figure 7c); fragments of the CNT meanders obtained at the conditions described above. From Figure 2 it is seen also that the construction of

FEC looks quite firm. The peculiar feature is that the height of the meander is lower than the height of the bulk CNT array (Figure 7c). It means that under the carried out conditions of CNTs synthesis, Ti electrodes suppress CNTs growth not only at their own surface, but also influence the rate of CNTs growth in the inter electrodes space. This difference in heights can partly or fully exclude the contribution of the meanders' area to overall emission by FEC of this type.

B. The structural characterization of CNT-based FECs on a dielectric substrate

The morphology of the CNT arrays was analyzed by SEM. In Figure 8 the morphology of the side-view (b) and the surface (b) of the CNT array are presented. It was revealed, that the surface and side-view morphologies of the arrays are similar both in the meander and bulk array areas.
As one can see in Figure 8a, CNTs are vertically aligned and tightly packed, except the surface of the array is strongly disordered (curly) (Figure 8b).

The structure and composition of CNTs in the arrays can be analyzed from Figure 9. According to Figure 9a, CNTs are multi-wall with the diameters in the range of 20-70 nm, most of them are filled with nanoparticles allocated in the channels (1) and in the walls (2) of CNTs.

In some cases they are located at the tips of CNTs (Figure 9b). These particles represent mostly cementite Fe_3C, some amount of Fe_5C_2 and different iron phases (XRD) (Figure 9c) [65-67].
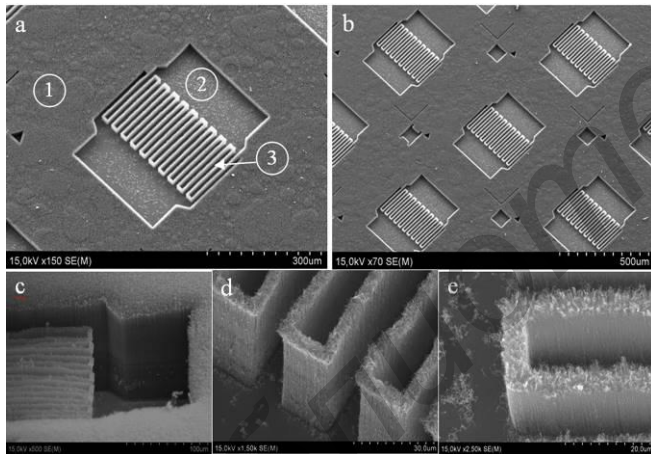

Figure 7: SEM images of the fragments of FEC active element, i.e. structured array of vertically aligned CNTs selectively synthesized on SiO_2 surface of Ti/SiO_2 topology at T=1150 K, v=1 см^3 min^{-1}; v_{N_2} =100 см^3 min^{-1} and other different parameters: (a,b,e) n=10%, t=0,5 min; (c,d) n=5%, t=1 min.
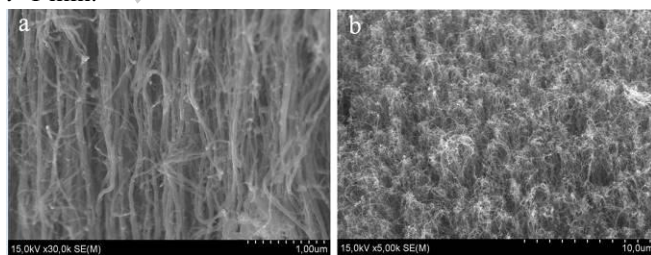

Figure 8: Morphology of the structured CNT array in bulk area: (a) side-view, (b) view of the surface of the CNT array

(SEM).

The construction of the passive and active elements of CNT-based FEC on a dielectric substrate, the morphology of the CNT arrays, the structure of CNTs in the arrays, as well as the parameters of the nanoparticles intercalated into the CNT arrays will influence the emission properties of FECs. However, the difference in heights of the CNT meander and bulk CNT array will be the crucial parameter influencing the emission characteristics of the FECs of this type.

C. The Field Emission Characteristics of the CNT-based FECs on a dielectric substrate

Since in the investigated FEC's construction the CNT arrays are synthesized on the dielectric SiO_2 layer, the electrical contact to CNT cathodes was realized by applying silver epoxy directly to the CNT array at a corner of the chip in such a way, that it was not protruding over the CNT array's surface. With such approach it is to determine the real FEC's emitting area, therefore under the integral measurements we operated with absolute value of current but not with the current density.

The field emission properties of the CNT-based FECs on the dielectric substrate were investigated for two types of specimens synthesized at the conditions mentioned above.

For the qualitative evaluation of the heights of CNT arrays over the chip area the optical profilometer (RFT MicroProf), which provides nondestructive measurements with micrometer resolution, was used.
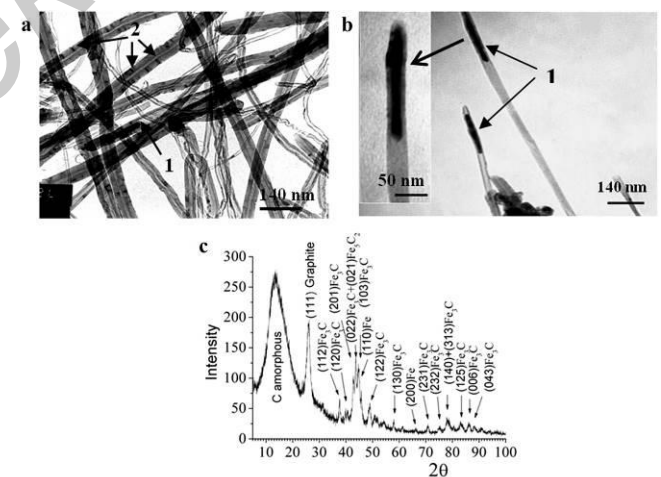

Figure 9: The structure and composition of CNTs in the arrays: (a) TEM image of CNTs with nanoparticles in their channels (1) and walls (2); (b) TEM image showing nanoparticles at the CNT tips (1); (c) XRD spectrum of CNT arrays.

One of the specimens (№1, Figure 7a) has the height of the bulk CNTs array of h1=60 µm and the height of CNT meander of h2=15 µm (the height difference, Δh, is 45 µm). In case of the second specimen (№2, Figure 7c), h1=120 µm, h2=105 µm, respectively (Δh=15 µm). Thus, in case of the specimen №1, the height difference is much larger than in the case of the specimen №2 what testifies to the diminishing influence of the Ti electrodes on the CNTs in the area of the meander-shape electrodes.

I-V curves and FN plots of specimens №1 (h1=60 µm) and №2 (h1=120 µm) in direct current (DC) mode in the "increase- decrease" voltage cycles are presented in Figure 11. The gap between anode and cathode electrodes gap was 300 µm. The value of applied voltage was restricted by the beginning of the luminescent layer destruction.

D. Field Emission Characteristics in Pulsed Mode

The FE characteristics of the specimens on the dielectric SiO$_2$ substrate № 1 and № 2 in pulsed mode after its testing in DC mode are presented in Figure 12. In pulsed mode, higher currents can be reached due to the significant decrease in the destruction process both of the specimen and luminescent screen, which is much more stable as being heated.

If the ratio of the pulse length to the pulse period is 10%, the screen heating duration is 10% while 90% time duration the screen is being "cooled down". The choice of the ratio is made experimentally, and depends on the screen material and the specimen under investigation. The value of the ratio does not influence the resulting emission current. In our case sample № 1 was measured with the duty cycle of about 30% (pulse length t=4 ms, pulse period T=14 ms) (Figure 12a), and for sample № 2 – of about 10% (pulse length t=2 ms, pulse period T=20 ms) (Figure 12c) [67].

Figure 10: 3D profiles of CNT-based FEC active element on the dielectric substrate: (a) general view, (b) the single FEC element (h$_1$ - the height of the bulk CNT array, h$_2$ – the height of the CNT meander).

Figure 11: FE characteristics in DC mode in the "increase-decrease" voltage cycles: (a,b) I-V curve and FN plot of the specimen №1; (c,d) I-V curve and FN plot of the specimen №2.

E. Analysis of the Field Emission characteristics

From Figure 11 it is seen that for the both specimens the FN plots calculated from the DC mode I-V curves are linear, what testifies to the field emission. The extreme values of the electric field intensity, Eex, and corresponding values of current, Iex, derived from the DC (Figure 11) and pulsed (Figure 12) mode I-V curves, as well as the calculated values of the field enhancement factor, β, for the specimens №1 and №2, are presented in Table 1.

F. Direct Current Field Emission Characteristics

As it is seen from Figure 11a and Table 1, in case of specimen № 1 Eex = 4 V/µm (which was reached before the luminescent screen material started to ablate), with the corresponding Iex~450 µA. In the case of specimen №2, Eex = 1,4 V/µm with Iex ~160 µA. The significantly lower value of Eex in case of specimen №2 testifies to the fact that emission is going on from the localized centers of FEC, what is leading to the local heating of the luminescent layer and its subsequent evaporation. Most probably, when the CNTs' height difference of Δh=15 µm (specimen №2) meanders contribute to the emission, while at Δh=45 µm (specimen №1) do not, and the emission originates from the edges of the structured CNT array, as well as from the surface of the bulk CNT array. As a result, specimen № 2 demonstrated higher FE efficiency than specimen № 1 (Figure 11a, Table 1).
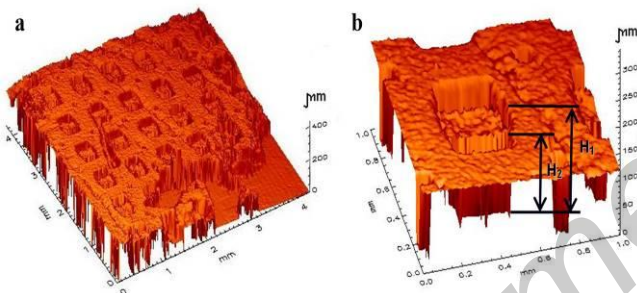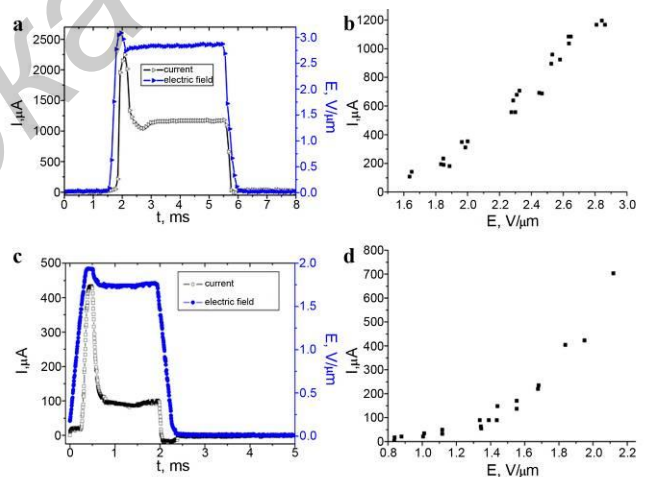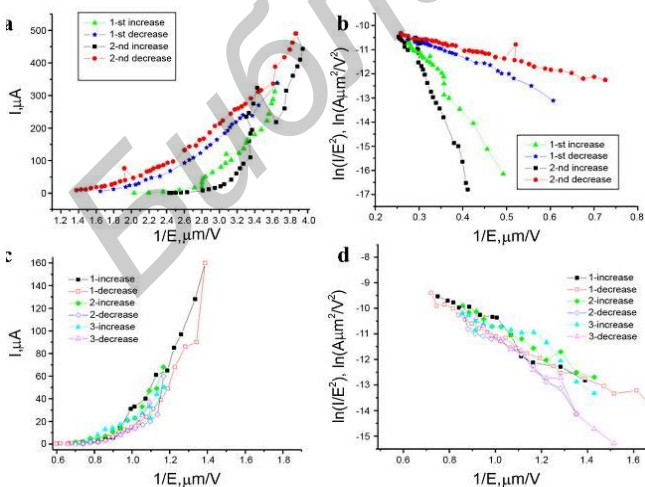

Figure 12: FE properties of the specimens № 1 (H1= 60 µm) and № 2 (H1=120 µm) in pulsed mode: (a,b) applied field E(t) versus resulting current I(t) pulses of the specimens № 1 и № 2, correspondingly; (c,d) I-V curves in the "increase-decrease" voltage cycles of specimens № 1 and № 2, correspondingly.

So, if for specimen №2 at Eex = 1,4 V/µm Iex ~160 µA (Table 1, columns 1,2); for specimen №1 under the same Eex the value of Iex is equal to only 20 µA (columns 3,4). Besides, the better emission characteristics of specimen №2 as compared to specimen №1 might be connected with the larger height of the bulk CNT array in case of specimen №2 (h1=120 µm), as compared to specimen №1 (h1=60 µm), i.e. aspect ratio of each separate CNT in the array would be higher, and as a result, its emission characteristics and field enhancement factor β would be higher as well.

The value of field enhancement factor calculated from the

experimental data is β=9917 for specimen №1, but for specimen №2 β=15250 (Table 1). This fact approves again higher emission efficiency of the specimen №2. Moreover, it is seen from Figure 11a,b that specimen №2 possess lower threshold field intensity (~0,7 V/μm), than specimen №1 (~2 V/μm).

Attracts attention the fact of different I-V curves behavior in the "increase-decrease" voltage cycles of specimens №1 and №2. In case of specimen №1, there is a big difference between increase-decrease cycles in I-V curves, while for specimen №1 this difference is insignificant. Evidently, this caused by the high working voltage and current in the case of specimen №1, what leads to the stronger burning-out of CNTs.

G. Pulsed Mode Field Emission Characteristics

In Figure 12a,c in E(t) and I(t) dependences at the beginning of the rectangular pulse of voltage, and, correspondingly, current, the peaks are observed. These peaks are determined by a ballast resistor which protects the IMLS

The mode of measurement	Specimen №	Eex, V/μm	Iex, μA	E, V/μm	I, μA	β
		1	2	3	4	5
Direct Current	№1	4,0	450	1,4	20	9917
	№2	1,4	160			15250
Pulsed Voltage	№1	3,0	1200	2,2	400	12685
	№2	2,2	750			26524

Table 1: The extreme values of the electric field intensity, Eex, and corresponding current, Iex, and the field enhancement factor, β.

against discharge, thus causing a small effective voltage reduction between the electrodes for increasing pulse current. The resulting current drop is more pronounced due to the nonlinear FN behaviour.

As it is seen from Figure 12b and Table 1, the extreme field intensity, Eex, for the specimen №1 in pulsed mode is 3,0 V/μm at which I~1200 μA, while in DC mode it was Eex=4 V/μm, I~450 μA.

From Figure 12d and Table 1 it is seen that for the specimen №2 Eex was improved, and is 2,2 V/μm with the current I~750 μA, while in DC mode it was Eex=1,4 V/μm and I~160 μA.

Comparing the data in Figure 12b and Figure 12d and Table 1, it is seen that specimen №2 demonstrates higher emission efficiency than specimen №1. In particular, for specimen №2, at Eex=2,2 V/μm, I~750 μA (columns 1,2), while for specimen №1 at the same Eex, I is only ~400 μA (columns 3,4).

The calculated integral field enhancement factors, β, are 12 685 and 26524 for specimen №1 and №2, respectively (Table 1), what once again confirms better emission characteristics of the specimen №2 in pulsed mode.

I-V curves of specimen №1 and №2 in pulsed mode in the "increase-decrease" voltage cycles almost do not change (Figure 12a,d). It might be connected with the following: the week spots were burned-out in DC mode; there are less

destruction caused by heating both of the luminescent screen and the specimen itself in pulsed mode, as compared to DC mode.

H. Local Field Emission FESM Characteristics

Local FESM measurements were performed with the 10 μm diameter anode tip and cathode-anode spacing of about 100 μm. The typical I-V curve of emitters is given in Figure 13.

Stable FN emission is typically observed up to some nA, as shown in the inset of Figure 13. The maximum local field emission current of CNT emitters was limited to 5-20 nA by unstable emission which often led to big current jumps or emitter destruction. The resulting mean β value of about 3200 corresponds to the geometrically calculated $β_{geo}$ value of about 3500, and depends on the aspect ratio of nanotubes. For typical CNTs, these locally measured β values are more representative than the integral ones (see below) governed by the strongest emitting sites.
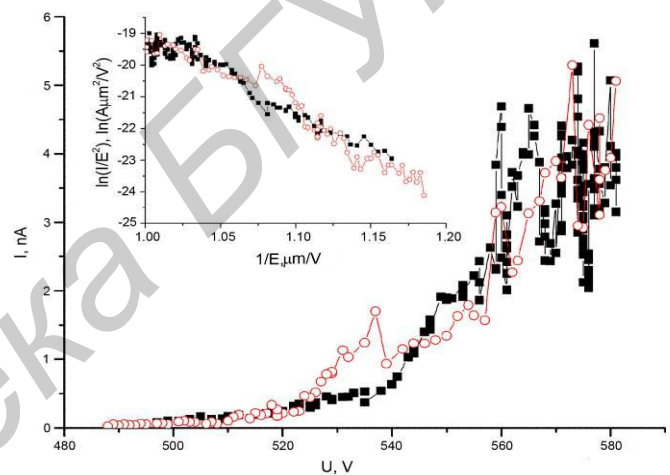

Figure 13: Locally measured typical I-V characteristic and corresponding FN plot (inset) of the emitting sites of specimen №2 (h_1=120 μm) at E=1,166 V/μm, I=68 μA.

I. Integral Field Emission Measurements in DC and Pulsed Modes

In our investigation a special attention was paid to the resulting IMLS images in DC and pulsed modes. The resulting IMLS images in DC mode in case of specimen №1 were obtained at Eex=2,65 V/μm, current I=143 μA, and in case of specimen №2 at Eex=1,166 V/μm, I=68 μA. As it was mentioned earlier, the applied voltage was restricted by the start of the luminescent layer destruction. In pulsed mode, the resulting IMLS images, as in case of field emission measurements, for sample №1 were obtained at duty cycle of about 30% (pulse length t=4 ms, pulse period T=14 ms), and for sample №2 - about 10% (pulse length t=2 ms, pulse period T=20 ms)

The main parameters characterizing IMLS images are the exposed area of the luminescent screen (area of luminous spots) and its brightness. For quantitative characteristics of the exposed areas the software package "Video TesT-Structure 5.1" was used [69].

Accentuation of the luminous spots on the IMLS images was carried out automatically by separating the images into a number of areas with similar color characteristics (color

diapasons). The general number of accentuated color diapasons, 3, the number of diapasons corresponding to the color of IMLS images - 1.

In Figure 14 the IMLS images of the investigated specimens with the automatic accentuation of the luminous spots are presented: (1) specimen №1 in DC mode, (2) specimen №2 in DC mode, (3) specimen №1 in pulsed mode, (4) specimen №2 in pulsed mode. In the left part of the program windows, the initial images are presented, and in the right part the automatically accentuated objects are represented (in red).

The parameters of the IMLS images of the investigated specimens are presented in Table 2. The values of the measured parameters characterizing IMLS images are presented in Table 3.
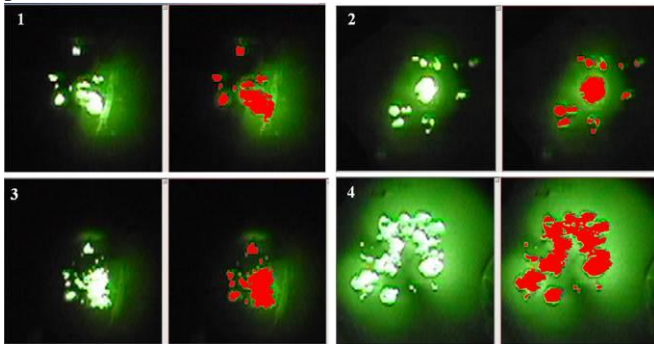

Figure 14: IMLS images of the investigated specimens with the automatic accentuation of the luminous spots: (1) specimen №1 in DC mode, (2) specimen №2 in DC mode, (3) specimen №1 in pulsed mode, (4) specimen №2 in pulsed mode.

Parameter	Formula	Remark
1. Area		The area of the luminous spots (not considering internal voids)
2 Average brightness	$B = \dfrac{\sum_{i=1}^{n} I_i}{n}$ where I_i– brightness of one point, n – number of points of the object	Average brightness of the luminous spots calculated as the sum of the brightness of all points of an object divided into the total number of points of this object.
3.Total integral brightness	$I = \sum_{i=0}^{n} I_i$	The total integral brightness is the sum of the brightness of all points of luminous spots.

Table 2: The parameters of the IMLS images of the investigated specimens.

Mode of the FE measure	Num ber of the	Parameters of measurements		
		Total area of	Average brightness	Total integral

ment	IMLS image	the luminous spots	of the luminous spots in brightness units	brightness of the luminous spots in brightness units
Direct current	1	24212	176+22	5137950
	2	23322	189+19	5011630
Pulsed	3	26922	179+31	5994836
	4	79494	185+19	17846252

Table 3: The values of the measured parameters characterizing IMLS images.

J. Integral Field Emission Measurements in Direct Current mode

As it is seen from Figure 14 and Table 3, the exposed spots' areas of the luminescent screen determined by the number of the emitting points (integral areas of the luminous spots), in the case of specimens №1 and №2 (in DC mode, images 1 and 2, correspondingly) are almost equal. The average and the total integral brightness have very small difference as well as.

The IMLS images in the case of specimens №1 were obtained at much higher Eex=2,65 V/μm and current I=143 μA than in case of specimen №2 (E=1,166 V/μm and I=68 μA). It means, again, that the emission effectiveness of specimen №2 is higher than of specimen №1.

K. Integral Field Emission Measurements in Pulsed Mode

In pulsed mode in case of specimen №1 (image 3), as compared to specimens №1 and №2 in DC mode, the total area of the luminous spots a little larger, medium brightness almost does not differ, and the total integral brightness is much higher.

Specimen №2 is quite distinguishable by its characteristics in pulsed mode (image 4). It is characterized by the approximately triple total area of the luminous spots and total integral brightness (79494 and 17846252, correspondingly) as compared to all the other cases, at approximately the same medium brightness.

The comparison of the presented data witnesses that in the case of both specimens the emission efficiency is higher in the pulse mode, especially in case of specimen №2.

Comparison of DC with pulsed IMLS images shows that the pulsed operation leads to the activation of CNT emitters, what results in higher homogeneity and enhanced field emission current at the same electric field.

V. CNT-BASED FECs ON A CONDUCTIVE SUBSTRATE

Practically, in all applications of CNT-based FECs [2-14] besides high current density, the homogeneity and stability of FE are required. The FE homogeneity and stability of flat CNT cathodes, however, are still limited by rather fast and uncontrolled growth of CNTs [70] which usually leads to strongly varying field enhancement and current carrying capability of the individual emitters [71, 72]. Therefore, the pillared CNT arrays having multiple individual emitters on

top and reduced mutual shielding [73] might provide a suitable strategy to improve the homogeneity and current stability of CNT-based FECs.

Pillared arrays of aligned carbon nanofibers can be easily fabricated on catalyst patterns by localized catalyst CVD, but it suffers from limited emission efficiency [74, 75]. Our sparsely-grown non-aligned, but well-anchored CNTs synthesized by ferrocene CVD in porous alumina templates resulted in high emitter number and current densities [76], but rather brittle cathodes of irregular shape unsuitable for triode applications.

In this section the systematic results on the FE properties of structured CNT arrays with different shape of pillars are reported. Pillared CNT arrays were preferentially grown on the flat patterned n-Si/SiO2 substrates by the atmospheric pressure floating catalyst CVD technique using ferrocene/xylene mixture [77, 78]. Spatially resolved, as well as integral FE measurements of the test array cathodes will demonstrate both high efficiency and high current capability, especially for long embedded CNT pillars. Long-term current stability and gas exposure tests will also be discussed.

A. The Construction and Production Technology of CNT-based FECs on a conductive substrate

The developed construction of CNT-based FECs on the conductive substrate is composed of the passive element: patterned Si/SiO$_2$ substrate with the cylindrical shape holes in SiO$_2$ layer, and the active element: structured CNT arrays of columns shape selectively grown on Si surfaces in the holes of SiO$_2$ layer.

The passive element of CNT-based FEC was produced in a following way. Low-resistivity silicon substrates (n-Si, 1 $\mu\Omega$cm) of 6x6 mm^2 size were thermally oxidized at 1100ºC in oxygen atmosphere. In the resulting SiO$_2$ oxide layer of 0,3 μm thickness the cylindrical shape holes of different diameters were opened by means of photolithography and selective chemical etching. As a result, Si/SiO$_2$ topology was created with the cylindrical shape holes in the SiO$_2$ layer with Si surface at the bottom of the holes.

The active element of CNT-based FECs on Si substrate was obtained by the selective CNT growth on Si surfaces in the holes of SiO$_2$ layer of Si/SiO$_2$ topology. As a result, the structured CNT arrays of columns shape were formed.

As in the case of CNT selective growth on Ti/SiO$_2$ described in section 4, the atmospheric pressure CVD method of CNTs synthesis was used by the high temperature pyrolysis *p*-xylene in the presence of volatile catalyst ferrocene with the same chosen parameters influencing the process of CNT growth. A systematic multiple-factor experiment have been carried on, which has given the possibility to determine the concrete conditions of the selective growth of the pillared CNT arrays on Si surfaces of Si/SiO$_2$ topologies [64]. Two types of specimens were investigated, which were produced at the same conditions, except the different synthesis time – 30 s and 2 min [78].

A special construction of CNT-based FECs represents a 5x5 mm^2 chip. It contains four 2x2 mm^2 areas with structured CNT arrays in a shape of columns (pillars). These pillared CNT arrays have different ratio of the distance between pillars, H, to pillar's diameter, d_p, in particular, 160/50,

100/30, 100/50 and 100/10 μm. In Figure 15 the fragment of the chip is presented.

Magnified side-view SEM images of the CNT pillars grown on Si surface of Si/SiO$_2$ topology are presented in Figure 16a, b. The CNT pillars in Figure 16a and b have same diameters, 30 μm, but different height, 20 μm and 50 μm (they were grown accordingly at duration of 30 s and 2 min). The pillars represent vertically aligned densely packed CNTs which are surrounded by a cloud-like floor of shorter CNTs which still grow on SiO$_2$.

TEM analysis showed that CNTs in the pillars are multi-wall, entangled and have diameters up to 80 nm. At the top of the pillars some multi-wall CNTs of 5-15 nm diameter and up to 5% overlength are discovered.

According to the factor of four of the chosen growth times, the short CNT pillars have a background cloud-like floor CNT layer of a few micrometers thickness, while in case of the long CNT pillars, on SiO$_2$ surface the 30 μm length CNT array of aligned nanotubes was formed.
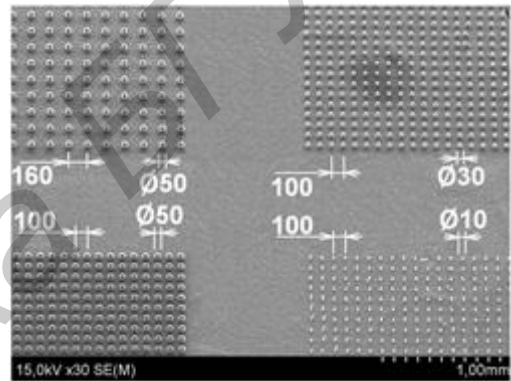

Figure 15: SEM image of the fragment of the chip, containing four FECs of pillared CNT arrays synthesized on the Si surface of Si/SiO2 topology (dimensions are given in μm).
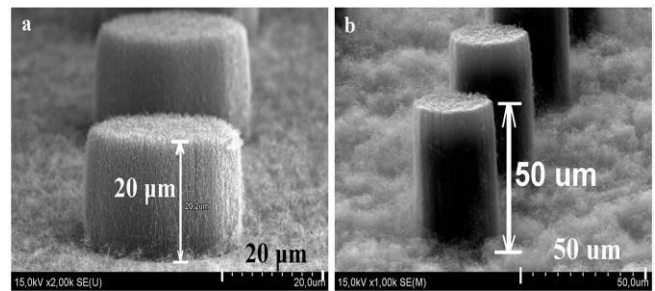

Figure 16: Side-view SEM images of 30 μm diameter CNT pillars grown on Si surface: (a) short pillars (20 μm) and (b) long pillars (50 μm).

B. Field Emission characteristics of the CNT-based FECs on a conductive substrate. Low, medium and high resolution FESM maps

Low resolution FESM maps of the FECs with structured CNT arrays having 20 μm diameter pillars (Figure 17) confirm a fairly homogeneous emission from the pillared CNT arrays' regions, but less pronounced FE occurred between the arrays too.

The dimensions of FECs are shown in Figure 15. The

typical medium resolution FESM maps (0,5 mm^2 scan area) of each of the four FECs shown in Figure 18, demonstrate that well-aligned and efficient FE from nearly 100% of the pillars was achieved at the electric fields below 15 V/µm.

The FESM maps, however, reveal the presence of some emitters between the pillars too. Moreover, multiple emitters, especially for 50 µm diameter pillars, are clearly visible already in the medium resolution (Figure 18c), as well as in the high resolution FESM maps.

Typical low and high resolution FESM maps of the structured CNT-based FECs on a chip with long CNT pillars (50 µm) are shown in Figure 19.

The FECs emitted at electric fields below 10 V/µm, but some pronounced FE occurred again between the pillars and structured CNT areas resulting in less uniform emission (Figure19b, c). In comparison, the emission from FECs with CNT pillars of 50 µm height is less homogeneous than from those with 20 µm height, due to the thicker CNT floor on SiO$_2$ which eventually causes strong FE, too. Therefore, the selectivity of the CNT growth process should be further improved especially for triode devices requiring low gate currents.
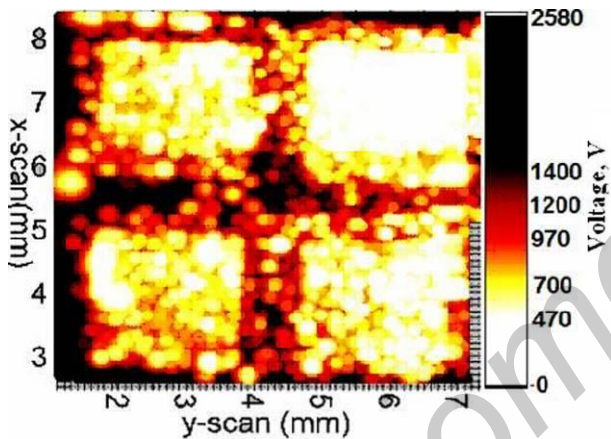

Figure 17: (Color online) Regulated voltage map for 1 nA current FECs on a chip with structured CNT arrays having 20 µm diameter pillars (scanned area 36 mm^2, low resolution anode with the diameter Ø 30 µm, cathode-anode gap 40 µm).
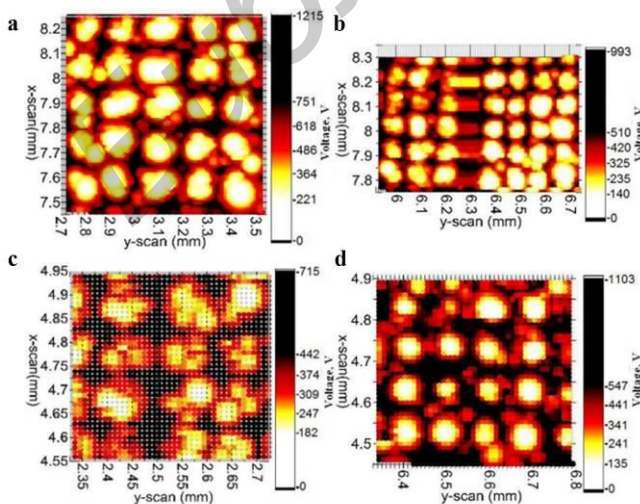

Figure 18: (Color online) Medium resolution regulated voltage maps (for 1 nA current, anode Ø 8 µm, cathode-anode gap 20 µm) of the same FEC on a chip as in Figure 12 (20 µm CNT pillars): (a) 0,64 mm^2; (b) 0,44 mm^2; (c) 0,2 mm^2; (d) 0,64 mm^2 quadrants.

A. Integral I-V curves

Integral characteristics of a single patch are presented in Figure 20. In particular, the integrally measured I-V curves of single CNT pillars with a Ø30 µm anode exhibited rather stable FN behavior up to currents of 80 µA for 20 µm CNT pillars, and excellent stability up to 500 µA maximum current for 50 µm CNT pillars, at electric fields up to 30 V/µm, as shown in Figure 20a.

It is remarkable that the current carrying capability of the short pillars, i.e. 20, 40 and 80 µA, strongly increased with their diameter (10, 30 and 50 µm, resp.), while for the longones it was only limited by the maximum range of the picoamperemeter (0,5 mA). This surprising result with respect to the current limits of a single multiwall CNT of about 20 µA [71, 72] might be explained either by a contribution of many entangled CNT emitters to the pillar current, or by their improved embedding in a highly conductive CNT floor, especially for the long pillars. In Figure 20b the field enhancement factor (of the randomly chosen pillars of both lengths are compared (at the assumed work function for CNT of 4,9 eV [79]). The short CNT pillars
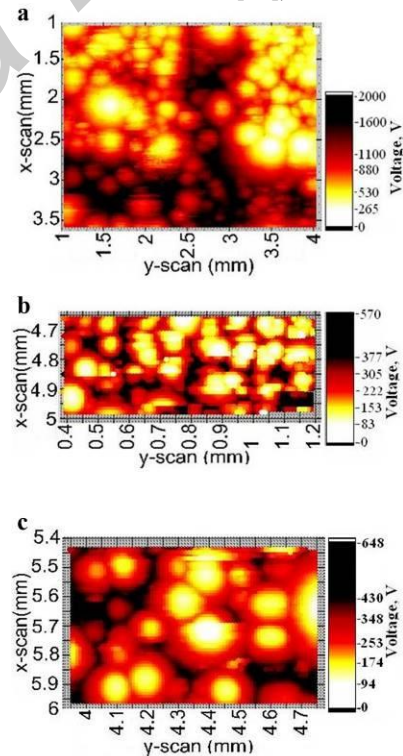

Figure 19: (Color online) Regulated voltage maps (for 1 nA current) of FECs on a chip with structured CNT arrays having 50 µm diameter pillars: (a) two upper quadrants corresponding to Figure 15 (scanned area 7,5 mm^2, low resolution anode Ø 30 µm, gap 60 µm); (b) lower left (0,28 mm^2); (c) lower right quadrant (0,64 mm^2) in high resolution (anode Ø 3 µm, gap 15 µm).
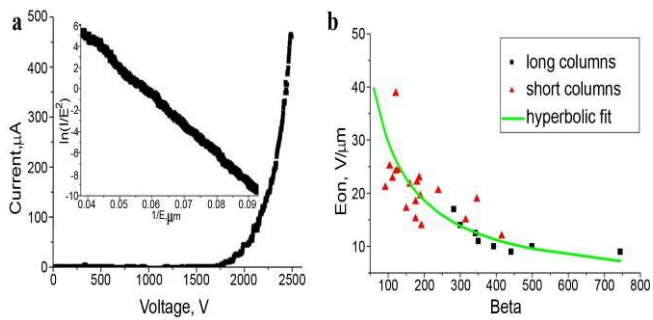
Figure 20: (a) Typical I-V and corresponding FN plots (inset) of a single CNT pillar (Ø 50 μm, 50 μm height) measured with the tip anode of Ø 30 μm showing excellent stability up to the maximum current of 500 μA; (b) Threshold electric field Eon (for 1 nA) vs. field enhancement factor eff plot for CNT-based FECs of both length for Ø 50 μm CNT pillars showing the expected hyperbolic correlation.

provided a larger distribution of β and electric threshold field values, while the long ones confirmed the hyperbolic correlation expected from the FN theory for a given current. Mean β values of 168, 111 and 185 (400) resulted for short (long) CNT pillars of 10, 30 and 50 μm diameter, respectively. These β values can not be explained by the ratio of the CNT pillars height and CNT radius but hint at varying mutual shielding effects [73] within the pillars and field enhancement by the outstanding individual CNTs.

B. Integral IMLS

The integral performance of the same structured cathodes with short and long CNT pillars was tested with the IMLS. In Figure 21 the current distribution over FECs obtained in DC and pulsed mode is displayed in luminescent screen images.

Fairly good FE current homogeneity is visible already at electric fields below 10 V/μm from all FECs, i.e. independent of the distance between to pillar's diameter pillars, H/dp, ratio. It should be mentioned that this result was achieved only after some pulsed mode processing of initially strong emitters at the edges of the cathodes. Obviously, the bright spots corresponding to resolvable emitters (20 μm) at low field levels (see Figure21c) smear out for higher currents due to the very bright halo produced within the luminescent screen (see Figure21d). The highest achievable cathode current of 81 (98 μA) in DC and 2,5 (10) mA in pulsed mode for short (long) columns, and it was always limited by the power load of the luminescent screen which caused some sulfur evaporation of the luminescent screen (as detected by the mass spectrometer) and risks successive cathode destruction by plasma discharges. Nevertheless, the achieved pulsed current density of at least 1,8 (40) mA/cm2 for the cathodes with short (long) CNT pillars can be derived. For the full exploitation of optimized CNT cathodes, therefore, metallic anodes will be required.

Long-term stability tests for both cathode types have been performed in DC mode for some hours under various vacuum conditions (Figure 22). As expected, much better stability was obtained for the longer CNT pillars as shown in Figure 22a.

At the base pressure of 2×10^{-7} mbar a strong activation of

emitters was observed, especially during first 20 minutes, which can be explained by the desorption of gases and/or electric field alignment of CNTs [52]. In contrast, the integral FE current decreased slightly under nitrogen, and strongly under oxygen exposure, which was done in four steps (at 10^{-6} mbar, 3×10^{-6} mbar, 10^{-5} mbar and 3×10^{-5} mbar) for 1 hour each. The effects summarized in Figure 22a can be probably explained by passivation due to adsorption of gas molecules (reversible effect) and bombardment of CNTs with ions leading to partial destruction of CNTs, especially in case of oxygen (irreversible effects). Various ions might also activate the FECs by splitting of the CNT bundles or sharpening of the tips or by removing adsorbates [80-82]. The current spike in the I-V curve for highest O_2 pressure (Figure 22a) was caused by a local spark as suggested by the corresponding IMLS images. Since the irreversible effects are mainly caused by oxygen, one operation hour at $3x10^{-5}$ mbar with O_2 gas would correspond to about 10000 hours at the base pressure of $2x10^{-7}$ mbar with 35,3% of H_2O as a main source of oxygen. In Figure 22b the permanent processing effects of both gases are compared by means of the integral I-V curves of the cathode. While the hysteresis effects at low fields confirm the emitter activation and passivation by desorption and adsorption of gases, a partial destruction of emitters leading to a shift to higher fields for the same current occurred only for oxygen processing.
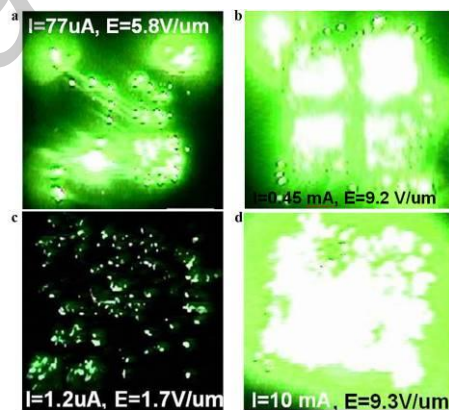

Figure 21: (Color online) The luminescent screen images of the structured cathode with short (a,b) and long (c,d) CNT pillars (arrays position correspond to Figure 15) in DC (a,c) and pulse modes with duty cycles of 2:20 ms (b) and 1,5:150 ms (d).
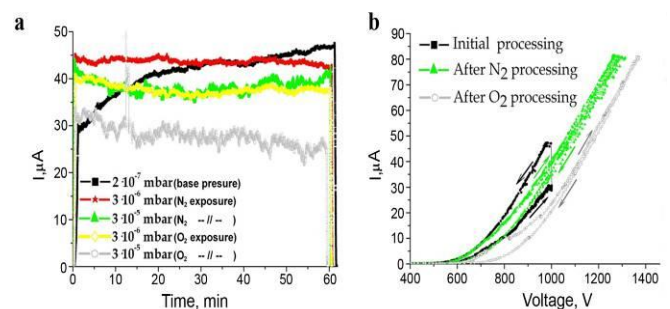

Figure 22: (Color online) Long-term stability tests: (a) integral long-term current stability of FEC with long CNT pillars at constant supply voltage (1 kV, 2.1 MΩ ballast resistor) measured at base pressure ($2x10^{-7}$ mbar) and at

enhanced partial pressures of nitrogen or oxygen; (b) integral I-V curves (300 μm gap) at base pressure showing processing effects for different gases (arrows indicate up- and down cycles).

The balance between passivation and activation of emitters was always depicted by the IMLS images, which revealed short-term current fluctuations for less than 20% of the spots and their partial redistribution at comparable current levels. In order to demonstrate the effects of current processing and gas exposure, averaged consecutive IMLS images (10 over 1 s) of the initial and final status have been subtracted by means of software image analysis. The result for the cathode with long CNT pillars for 10 μA integral current is shown in Figure 23. After full processing time, 12% of the emitting area remained stable, while 44,3% (43,6%) has been activated (deactivated). Considering the moderate field values chosen to avoid the halo effects mentioned above, this result supports our strategy to improve the homogeneity of structured cathodes by multiple CNT emitters per pillar.
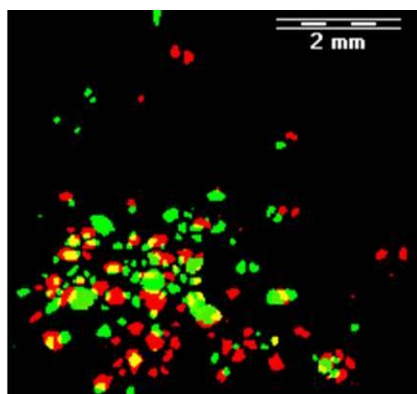

Figure 23: (Color online) Software analysis of the IMLS images obtained for 10 μA integral current initially (at 785 V) and finally (at 900 V) for the same cathode as in Figure 14 showing the processing effects of both gases. The emitter distribution has partially changed resulting in stable (yellow), activated (green) and deactivated (red) emitters.

VI. FIELD EMISSION CATHODES BASED ON POROUS ANODIC ALUMINA AND CARBON NANOTUBES

A. Influence of contact interfaces between the carbon nanotubes and Si substrate on field emission properties of CNT arrays in PAA

Large-scale arrays of CNT on conductive substrates as the field-emission cathodes have attracted considerable interest due to their potential applications in areas such as electronics, optoelectronics, sensing, and especially ultra-thin flat display devices [83]. In order to tailor the properties of the CNTs in the matrix of FECs it is necessary to create an array with tunable size, shape, and spacing of vertically oriented CNT, using patterning techniques. The most widespread way of orientation and location of CNT array is using of nanoporous templates [84] such as self-organized porous films of porous anodic alumina (PAA) [84, 86]. PAA films have unique cellular-porous structure representing hexagonally packed cells with vertical pores. The sizes of PAA cells and pores can

be controllably varied over a wide range by changing the anodizing conditions. However, to realize such structures is necessary to solve two problems - to remove dielectric barrier oxide layer in the bottom of pores and instead to create a conductive interface to allow contact between the CNT and the substrate [87]. It is important to ensure good electrical contact with the conductive nanotubes formed substrate.

We proposed three variations of forming systems nanocontacts (interfaces) in the pores of PAA based on electrochemical technology providing well-controlled growth of the films at low temperatures [88]. The first method is based on the local oxidation of Ti-underlayer through a mask PAA (type 1- interface TiO_2 /Ti) [89], the second - on the selective oxidation of Si-substrate (type 2- interface SiO_2) [90], and the third - on the electrolytic deposition of Ni into the pores of the PAA (type 3- interface Ni) [91]. To provide the necessary regularity obtained nanocontacts the forming of highly ordered PAA matrix was carried out at the electrochemical conditions, which provided the required morphology and nanostructure [92].

In order to grow thin uniform PAA films, Al/Ti metal bilayers (1,0/0,25 μm thick for type 1) and Al layers (1,5 μm thick for types 2 and 3) were sputter-deposited on 100-mm single-crystal Si (100) wafers (n-type, 4,5 Ω cm). The use of the silicon wafers was essential for a uniform electric field distribution and low-resistive electron supply across the Al/Si interface during later anodization, especially when the Al_2O_3/Al interface approaches the Si surface. Anodization was performed in 0,2 M oxalic acid electrolyte in a two-electrode cylindrical cell at room temperature. A P5827M potentiostat (Belarus) was used as the anodizing unit. To obtain PAA films with pores of about 40 nm in diameter, anodization at 48 V was performed in a constant current mode. The process was stopped when the pores in the alumina film reached the Ti layer (type 1) or the Si substrate (type 2), which thereby were slightly oxidized to TiO_2 or SiO_2, respectively, with the formation of corresponding oxide "nanohillocks", of about 5 nm in height. In type 1 interface, the titanium underlayer was then reanodized to a voltage of 55 V, which initiated the growth of TiO_2 nanopillars, of about 100 nm in height. Annealing the samples in vacuum at 450ºC for 2 hours minimized the resistance of type 1 interface [93]. Then the pores in the alumina films were widened to a diameter of about 45 nm (interpore distance ~ 120 nm) by chemical etching in 2 M H_2SO_4 at 50ºC for 30 minutes. For type 3 interface, a layer of Ni catalyst, of about 200 nm in thickness, was electrochemically deposited into the pores in a mixture of 0,38 M $NiSO_4$, 0,13 M $NiCl_2$ and 0,65 M H_3BO_3 (pH 5.2) at 4 mA/cm^2 and 45ºC for 3 minutes. Cross sections and surfaces of the specimens were examined by scanning (SEM) and transmission electron microscopy (TEM). SEM images of the prepared specimens are shown in Figure 24.

CNTs were synthesized by low-pressure CVD in the PAA pores with various contact interfaces. Pyrolysis of fluid hydrocarbon xylene with 1% volatile ferrocene in Ar flow as carrier gas at 850ºC for 30 seconds was used. The structure and size of the CNTs were investigated by SEM, TEM and Raman spectroscopy. The parameters of the synthesized nanotubes were examined by transmission and scanning

electron microscopy and Raman spectroscopy. As a result of the synthesis of the inner surface of the walls of each pore was coated with carbon from the contacts (interfaces) to the surface of the oxide [49, 94], forming multiwall nanotubes the same shape of pores (Figure 25b). Contacts between the substrate and the nanotubes provided by the one of three types of interfaces. Moreover, the growth of random nonaligned multiwall CNTs with a diameter of up to 100 nm and a length of up to 5 µm was observed for the uniform (patterned) samples, especially along the edge of the specimen (Figure 25b).

The integrated field emission (FE) properties of the CNT nanotube arrays were measured in direct and pulsed current modes using FESM for spatially resolved measurements and IMLS for application issues by the described above method (see section 4). We have investigated the influence of three different types of contact interfaces between the CNTs and the PAA-coated Si substrate – 1) TiO_2/Ti, 2) SiO_2 and 3) Ni/SiO_2 - on the FE properties [95].
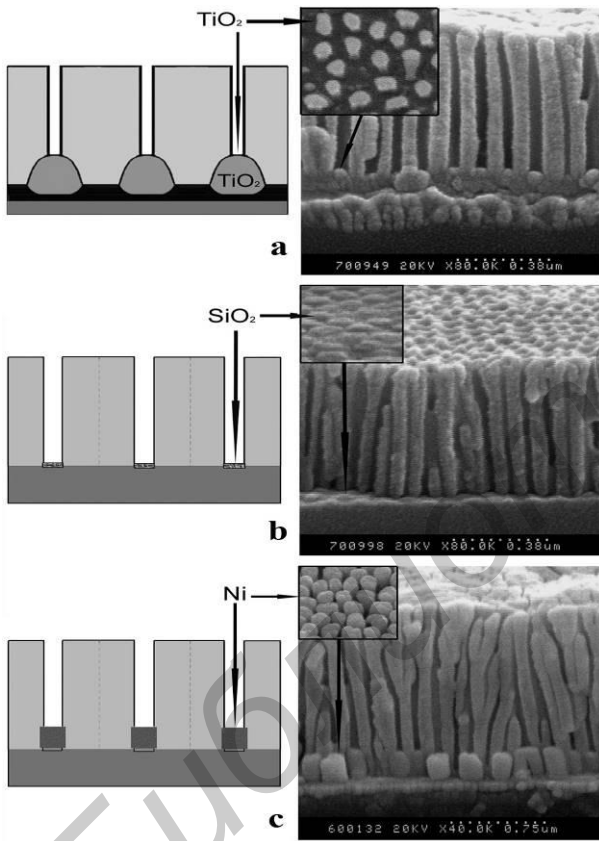

Figure 24: Three different CNT contact interfaces: (a) $Si/Ti/TiO_2$ (type 1); (b) Si/SiO_2 (type 2); (c) $Si/SiO_2/Ni$ (type 3).
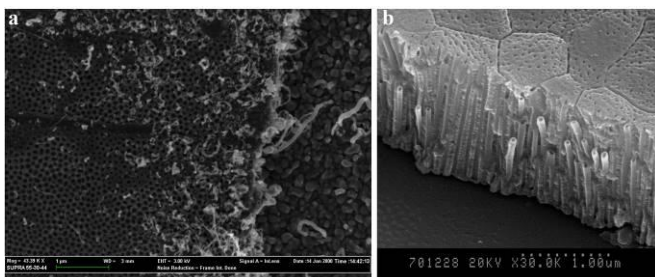

Figure 25: SEM images of CNTs on the perimeter surface (a) and in the middle (b) of uniform PAA matrixes.

In Figure 26a I-V characteristics are built in the normal coordinates for the three types of interfaces. As the graphs show the I-V characteristics have an exponential form, and the minimum threshold electric field pattern showed a third type of interface, which was 1,17 V/m at a current of 1 mA. The first type of interface has threshold electric field strength 1,73 V/m, while the second type of interface – 2,53 V/m. The level of field-emission current samples is located in the same sequence. The arrays of carbon nanotubes with the Ni/Si contact interface have the maximum current density [96], the structures with the $TiO_2/Ti/Si$ interface have slightly lower densities, and the minimum current density was in structures with the SiO_2/Si interface.

Figure 26b shows the current-voltage characteristics of these structures with coordinates Fowler-Nordheim. All characteristics had a linear dependence of the form, indicating that the classical quantum - mechanical FE mechanism. Minor deviations from the straight line due to various effects associated with the principles of integral measurements. After linear approximation graphs the field enhancement factors β have been calculated from the resulting Fowler-Nordheim plots for a work function of 4.9 eV for the three types of interfaces [97]. The third type of interface had maximum value of β equal 6499, the β factor of first type was 5974, and for the second type of interface β did not exceed 4830.

In order to resolve the local FE properties of all the CNT samples, FESM measurements were performed with a 30-µm diameter tungsten anode. In Figure 27, the maps of the regulated voltage which is required for a current of 1 nA demonstrate the presence of distributed emitters, which are stronger along the perimeter and weaker in the center of the samples. The corresponding threshold fields E_{on} for 1 nA vary between 1,5 and 10,0 V/µm. Local measurements of about 10 single emitters on each interface type provided FN curves with average E_{on}(1 nA) of 5±2,5, 12,5±4 and 4,7±1 V/µm and FN slopes corresponding to typical field enhancement factors β of 593, 246 and 618, respectively (Figure 28).
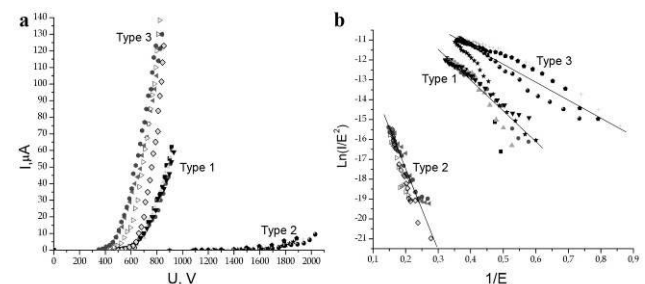

Figure 26: Integral I-V curves measured in dc mode (a) and corresponding FN plots (b).
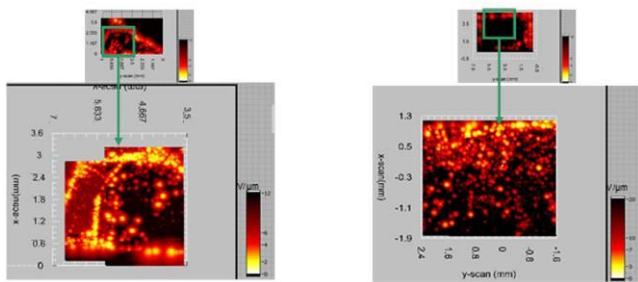
Figure 27: Low and medium resolution voltage maps for 1 nA of CNT samples.

Stable local currents up to 10,0, 2,0 and 10,0 µA, limited by slight saturation, were obtained from the strongest emission sites on type 1 - 3 interfaces. Therefore the CNTs on PAA-coated Si substrates with the TiO_2/Ti and Ni/SiO_2 contact interfaces provide a stronger and more stable electron emission than those on the SiO_2 contact interface.

Nonaligned CNTs anchored in the nanoporous PAA films on highly conductive Si wafers with the TiO_2/Ti and Ni/SiO_2 contact interfaces have demonstrated low FE thresholds (in average 5 V/µm for 1 nA) and high stable current limits (10 µA). Integral measurements of the uniformly coated samples revealed a strong edge emission with the current densities up to 10 mA/cm^2.
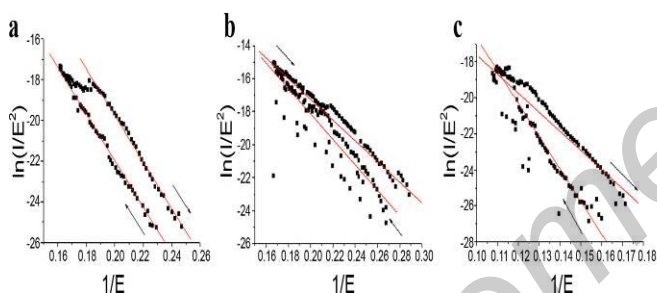

Figure 28: Typical FN plots of local emitters for type 1 (a), type 2 (b), type 3 (c) interface of CNT samples.

B. Matrixes FECs based on CNT in porous anodic alumina

Using photolithography and etching we created a matrix FECs based on CNT embedded into PAA with TiO2/Ti contact interface between the substrate and carbon nanotubes. The construction of FECs matrix contains four 2x2 mm2 areas with structured CNT arrays in a shape of columns with different diameters and distances between columns as shown in Figure 15. This design allows to prevent the shielding effect of close-CNT and to determine the optimum geometrical dimensions of the cathodes and the distance between them. Thus creating a matrix of field emission cathodes, which are columns c height of 1,500 microns and diameters of 10, 30 and 50 microns with different distances between them, and each column is a template of PAA with imbedded CNT [93].

The composition of carbon nanotubes in PAA investigated using the Raman spectroscopy. The Raman spectrum is present by two bands at 1600 cm-1 and 1345 cm-1 (Figure 29). First indicates that the resulting structures are multiwall

CNTs [98], ant second band corresponds to the vibrational states of the broken hexagonal crystal lattice near the boundary and indicates the presence of amorphous transitional forms of carbon (powdered graphite, carbon black) [86, 99].
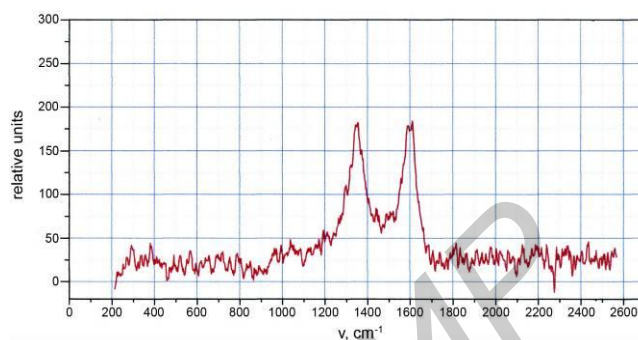

Figure 29: Raman spectrum OF CNT in PAA.

To study the distribution of concentrations of the major elements of the profile structures from the surface to the silicon substrate Auger analysis of the samples was performed (Figure 30). The spectrum shows the changes in concentrations of the major elements (aluminum - Al, oxygen - O, carbon - C, titanium - Ti, silicon - Si) in matrix of PAA with CNT. On the surface structure the C concentration is the highest, which is associated with CNT and nanometer thin carbon layer covering the surface of the porous matrix (see Fig. 20a), the thickness of which can be up to 50 nm. At the depth of 40-50 nm from the surface the C appear as partial structure of the oxide. Concentrations of O and Al remain approximately constant throughout the thickness of the oxide, C concentration also remains constant, which indicates the formation of carbon-containing tube that is located along the length of the pores [100]. At the bottom of pores the carbon concentration has decreased, and the concentration of metal oxide titanium appears and increases. The overlap concentration suggests that the carbon tube and a titanium interface make good contact, possibly with the formation of the carbide compound. Since the approach of carbon concentration to zero, on the spectrum the concentration of Si begins to appear, its concentration increases sharply with advancing inland. Silicon appears well before the front reaches the etching of the silicon substrate.

Important information from the Auger analysis is the ratio of the concentrations of atoms Al, O and C. So in the usual Al_2O_3 concentration ratio of Al and O is 2/3, which is equivalent to 40% Al to 60% O. After synthesis of CNT concentrations of Al and O, respectively, and reduced to 29% and 52%. This may be due to the fact that during the high-temperature synthesis on the inner surface of the pore walls is a restoration of Al and O oxide by carbon, and the oxygen escapes, and aluminum combined with carbon to form a carbide compound Al_4C_3 [100]. This is also confirmed by the data obtained by SEM, since the diameter of carbon nanotubes by an average of 10-15 nm, the diameter of the pores of the original matrix AOA.
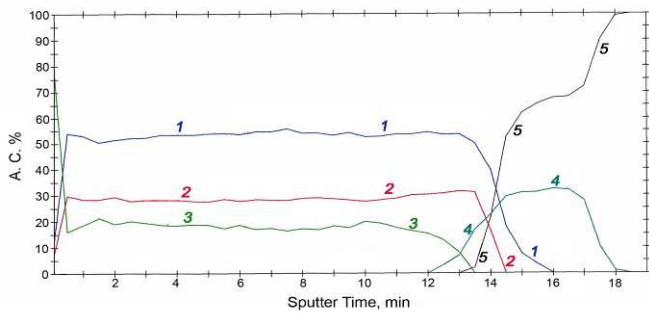
Figure 30: Auger analysis of the concentrations distribution of elements PAA with CNT: 1 – (O), 2 –(Al), 3 – (C), 4 – (Ti), 5 – (Si).

Field emission characteristics of the study carried out by the method described above. Initially, samples were tested in constant voltage mode, and then in the pulsed voltage, with a special emphasis on the uniformity of the electron emission from the FECs surface arrays. In Figure 31 shows photographs of the image data. As can be seen from the photos in the pulsed mode (Figure 31b) initiated a greater number of cold cathodes than with DC (Figure 31a). The photos show four regions corresponding to the four different arrays FECs. In constant voltage mode the emission current achieved to 563 µA/sm^2 at electric field strength of 4 V/m. In the pulsed the emission current exceeded to 130 mA/cm2 at a voltage of 5,9 V/m. This was due to a large number of emitters initiated, and with the ability to achieve high electric fields without significant sputtering phosphor covering the screen. Also Figure 31 shows a photograph of the screen, resulting in the emission of electrons from the surface of a single array in which FEC have diameters of 50 mm and are spaced 100 microns, from this photo one can see that emitted about 80% of FECs. In assessing the impact on the size of PEC phosphor luminescence intensity indicated that maximum radiation is observed in the segment with diameter of 50 mm and distance of 100 mm [101].
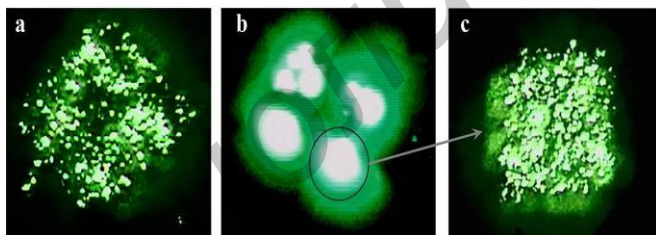

Figure 31: Photographs of the screen, resulting in the emission of electrons from the surface: (a) in DC mode, (b, c) in pulsed mode.

In Figure 32 are shown the current-voltage characteristics obtained in pulsed mode in normal coordinates and in the coordinates of the Fowler - Nordheim. As the plots show the characteristics have exponential form. At threshold electric field of 1,5 V/m for both modes of measurements the emission current was 1 mA. Following the restructuring of the I-V characteristics in coordinates Fowler - Nordheim (Figure 32b) graphics acquire a linear form, indicating the quantum mechanical nature of the electron emission, which

occurs in accordance with the theory of F - H, by the mechanism of electron tunneling through the narrowed field of electric potential barrier at the section of CNT - vacuum. Deviation from a straight line performance can be attributed to the gradual break-in structures and instant integral current fluctuations caused by changes in the geometry and spatial relationships of individual nanotubes in an electric field in the measurement process. The slope of the linear approximation in the theory of F - H was calculated the field enhancement factors β (9180 in DC mode and 11800 in pulse mode) [102].
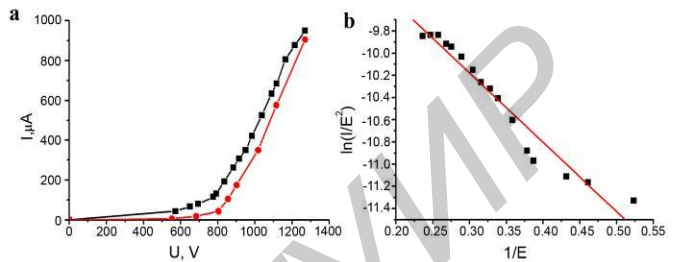

Figure 32: The I-V characteristics in pulsed mode in normal coordinates (a) and F-N (b).

VII. RESULTS AND DISCUSSION

The FE properties of the samples were investigated in direct current (dc) and pulsed modes of an integrally measuring diode system with luminescence screen (IMLS) at about 10-6 mbar as well as with a FE scanning microscope (FESM) at about 10-9 mbar [6]. Typical IMLS images of the unstructured samples (about 20 mm2 size, 300-µm electrode gap) showed many emission sites along the edge but only few sites in the specimen's center (Figure 26 3), thus corresponding to the distribution of CNTs in the PAA matrixes. In pulsed IMLS mode, the maximum current densities were 10,5 mA/cm2 (at 4,8 V/µm), 0,9 mA/cm2 (at 9 V/µm) and 4 mA/cm2 (at 4 V/µm) for types 1, 2 and 3, respectively. The integral current-voltage (I-V) curves in Figure 27 4 show an average Fowler-Nordheim (FN) behavior and current saturation effects, which are especially pronounced in the case of type 3 interface.

In order to resolve the local FE properties of all the CNT samples, FESM measurements were performed with a 30-µm diameter tungsten anode. In Figure27 5, the maps of the regulated voltage which is required for a current of 1 nA demonstrate the presence of distributed emitters, which are stronger along the perimeter and weaker in the center of the samples. The corresponding threshold fields Eon for 1 nA vary between 1.5 and 10.0 V/µm. Local measurements of about 10 single emitters on each interface type provided FN curves with average Eon(1 nA) of 5±2,5, 12,5±4 and 4,7±1 V/µm and FN slopes corresponding to typical field enhancement factors β of 593, 246 and 618, respectively (Figure28 6).

Stable local currents up to 10,0, 2.0 and 10,0 µA, limited by slight saturation, were obtained from the strongest emission sites on type 1 - 3 interfaces. Therefore the CNTs on PAA-coated Si substrates with the TiO2/Ti and Ni/SiO2 contact interfaces provide a stronger and more stable electron emission than those on the SiO2 contact interface.The IMLS

measurements of the first-structured samples (as shown in Figure 25 7a) were performed in dc and pulsed modes. The maximum current density achieved in both modes for the sample shown in Figs. 29 7b and 29 7c was 1,5 mA/cm2 at 8 V/µm and 4 mA/cm2 at 13 V/µm, respectively. Unlike to the unstructured samples, the emission homogeneity is significantly improved in the area of the four IDE patches. However, no difference between the fingers and the base regions of the IDEs were observed, and some emission occurred in the 1-mm spacings between the patches. Therefore, the expected localization of the CNT growth has been achieved only partly.

VIII. CONCLUSIONS

A number of constructions of the FECs on the basis of CNT arrays have been constructed and tested. In order to avoid the shielding effect caused by closely located CNTs in the array, a special technology of CNT arrays structuring had been developed. The structuring was realized by the selective growth CNTs of on the metal/semiconductor/dielectric surfaces. Three particular constructions of FECs are investigated: CNT-based FEC on the dielectric substrate, CNT-based FEC on the conductive substrate, CNT-based FEC on porous AAO/conductive substrate. The CNT arrays were synthesized by the atmospheric pressure floating catalyst CVD method under the high temperature pyrolysis of ferrocene/xylene solution. FE properties of FECs were measured in DC and pulsed modes, integrally and locally. All structured CNT-based FECs performed high FE properties, but with the peculiarities for each type of FECs.

The CNT-based FECs on the dielectric substrate was composed of a passive element, i.e. Si/SiO2 substrate with planar Ti interdigitated electrodes, and an active element, structured CNT array in the shape of meander in the inter electrodes space and bulk CNT array around Ti electrodes selectively grown on SiO2 surface. The technology of selective growth of the arrays of vertically aligned CNTs synthesized on SiO2 surface of SiO2/Ti topology was developed. CNT-based FECs on the dielectric substrate demonstrated low onset electric fields, but moderate uniformity of emission, which has to be optimized for displays application.

CNT-based FEC on the conductive substrate was composed of a passive element, i.e. patterned Si/SiO2 substrate with the cylindrical shape holes in SiO2 layer, and active element, pillared CNT arrays selectively grown on Si surfaces of Si/SiO2 topology. The technology of selective growth of the arrays of vertically aligned CNTs synthesized on Si surface of Si/SiO2 topology was developed.

Two types of specimens were investigated, which were obtained in the same conditions besides the different growth duration, 30 s and 2 min, what resulted in the different heights of the CNT pillars, 20 and 50 µm. A special construction of 5x5 mm2 chip with the CNT-based FECs on the conductive Si substrate was developed. Chip contains four FECs areas of 2x2 mm2 with pillared CNT arrays. These areas had different ratio of the distance between pillars, H, to pillar's diameter, dp, in particular, 160/50, 100/30, 100/50 and 100/10 µm.

FECs with short CNT pillars (20 µm) showed uniform and efficient FE from nearly 100% of the pillars at electric fields below 15 V/µm, but only moderate currents per pillar of up to 80 µA, which might be promising for triode applications. In contrast, FECs with long CNT pillars (50 µm) yielded stable currents of at least 0.5 mA, suitable for power devices. These high current values, as well as the derived field enhancement factors, suggest the presence of multiple CNT emitters per pillar. The fairly homogeneous cathodes with long columns provided the integral current density of up to 40 mA/cm2 at 10 V/µm in pulsed mode, which was limited by the power load to the luminescent screen. The long-term stability of FECs was proven by DC processing under enhanced oxygen pressure. Combining the reproducibly high and stable currents per pillar with the obtained high FE homogeneity, current densities in the range of A/cm2 can be expected for optimized cathodes with arrays of long CNT pillars of 50 µm diameter, 160 µm distance between the pillars, and 1 mm2 size.

The CNT-based FEC in porous AAO/conductive substrate is composed of the passive element, i.e. Si conductive substrate with the continuous or IDE patterned AAO layer on top, and the active element, CNTs grown in the pores of AAO layer on the conductive Si substrate by means of different catalyst contact interfaces. Nonaligned CNTs anchored in the nanoporous alumina layer on highly conductive Si substrate with the TiO2/Ti and Ni/SiO2 contact interfaces have demonstrated low FE thresholds (in average 5 V/µm for 1 nA), and stable current limits (10 µA). Integral measurements of the uniformly coated samples cathodes revealed a strong edge emission with the current densities of up to 10 mA/cm2. The growth of CNTs on the IDE-patterned alumina layer gave a reproducible, quite homogeneous FE distribution across the whole sample surface, which must be further improved for the triode applications.

REFERENCES

[1] Iijima S. Helical Microtubules of Graphitic Carbon. Nature 1991; 354(6348) 56-58.

[2] Choi WB, Chung DS, Kang JH, et al. Fully sealed, high-brightness carbon-nanotube field-emission display. Applied Physics Letters 1999; 75(20) 3129-3131.

[3] Heo SH, Ihsan A, Choa SO. Transmission-type microfocus x-ray tube using carbon nanotube field emitters. Applied Physics Letters 2007; 90(18) 183109-183111.

[4] Choi HY, Chang WS, Kim HS, et al. Acquisition of X-ray images by using a CNT cold emitter. Physics Letters A 2006; 357(1) 36-41.

[5] Liu Z, Yang G, Lee YZ, et al. Carbon nanotube based microfocus field emission x-ray source for microcomputed tomography. Applied Physics Letters 2006; 89(10) 103111-103113.

[6] Zhou O, et al. Generation of continuous and pulsed diagnostic imaging x-ray radiation using CNT FE cathode. Applied Physics Letters 2002; 81(2) 355-357.

[7] Reyes-Mena A, et al. Miniature X-ray tubes utilizing carbon-nanotube-based cold cathodes. Advances in X-ray Analysis 2005; 48 204-209.

[8] Legagneux P, Minoux E, Hudanski L, Teo K, Griening O, Peauger F, Dieumegard D, Schnell J, Gangloff L, Amaratunga G. GHz modulation of carbon nanotube cathodes for microwave amplifiers. IEEE 2005; 2: 865-7.

http://ieeexplore.ieee.org/xpl/login.jsp?tp=&arnumber=1500670&url=http%3A%2F%2Fieeexplore.ieee.org%2Fxpls%2Fabs_all.jsp%3Farnumber%3D1500670 (accessed 4 September 2012).

[9] Milne WI, Teo KBK, Minoux E, et al. Aligned carbon nanotubes/fibers for applications in vacuum microwave devices. Journal of Vacuum Science & Technology B: Microelectronics and Nanometer Structures 2006; 24(1) 345-348.

[10] Milne WI, et al. Carbon nanotubes as field emission sources. Journal of Materials Chemistry 2004; 14(6) 933-943.

[11] Leshukov MYu, Baturin AS, Chadaev NN, et al. Characterizations of light sources with carbon fiber cathodes. Applied Surface Science 2003; 215(1-4) 260-264.

[12] Wei Y, et al. Cold linear cathodes with carbon nanotube emitters and their application in luminescent tubes. Nanotechnology 2007; 18 325702-325707.

[13] Hozumi Y, Ohsawa S, Sugimura T, Ikeda M. Development of field-emission electron gun from carbon nanotubes. In: Proceedings of LINAC, 16-20 August 2004, Lubeck, Germany.
http://www-linac.kek.jp/linac-paper/2004/linac2004-hozumi-nanotube.pdf (accessed 4 September 2012).

[14] Kim SJ. Gas sensors based on Paschen's law using carbon nanotubes as electron emitters. Journal of Physics D: Applied Physics 2006; 39(14) 3026-3029.

[15] Quy NV, Hoa ND, Yu WJ, et al. The use of anodic aluminum oxide templates for triode-type carbon nanotube field emission structures toward mass-production technology. Nanotechnology 2006; 17 2156-2160.

[16] Shulitski B, Labunov V, Prudnikava A. High Efficiency Method of Selective CNT Arrays Growth on the Metal/Dielectric/Semiconductor Substrates for FEDs Application. In: Society for Information Display International Symposium: SID Symposium Digest of Technical Papers, 3-9 July 2006, San Francisco, CA, USA, 37(1), 644-647.
http://onlinelibrary.wiley.com/doi/10.1889/1.2433587/pdf (accessed 4 September 2012).

[17] Fowler RH, Nordheim L. Electron Emission in Intense Electric Fields. Proceedings of the Royal Society of London. Series A, Containing Papers of a Mathematical and Physical Character 1928; 119(781) 173-181.

[18] Burgess RE, Kroemer H, Houston JM. Corrected Values of Fowler-Nordheim Field Emission Functions v(y) and s(y). Physical Review 1953; 90(4) 515.

[19] Kim D, Bouree JE, Kim SY. Numerical study on the field emission properties of aligned carbon nanotubes using the hybrid field enhancement scheme. Applied Physics A 2006; 83(1) 111-114.

[20] Gröning O, Küttel OM, Emmenegger C, et al. Field emission properties of carbon nanotubes. Journal of Vacuum Science & Technology B: Microelectronics and Nanometer Structures 2000; 18(2) 665-679.

[21] Bonard JM, Croci M, Arfaoui I, et al. Can we reliably estimate the emission field and field enhancement factor of carbon nanotube film field emitters? Diamond and Related Materials 2002; 11(3-6) 763-768.

[22] Dyke WP, Dolan WW. Field Emission. Advances in Electronics and Electron Physics 1956; 8 89-185.

[23] Lysenkov D. Optimization of nanostructures for field emission cathodes. PhD thesis, WUB-DIS 2006-02, University of Wuppertal; 2006.

[24] Pupeter N. Untersuchung der überhöhten Elektronenfeldemission an chemisch und mechanisch polierten Nb-, Nb3Sn-, Cu- und Al-Oberflächen in Verbindung mit Heizbehandlungen. PhD thesis, WUB-DIS 96-16, University of Wuppertal; 1996.

[25] Mahner E, Minatti N, Piel H, Pupeter N. Experiments on enhanced field emission of niobium cathodes. Applied Surface Science 1993; 67(1-4) 23-28.

[26] Wang T, Reece CE, Sundelin RM. Enhanced field emission from chemically etched and electropolished broad-area niobium. Journal of Vacuum Science & Technology B: Microelectronics and Nanometer Structures 2003; 21(4) 1230-1240.

[27] Egorov NV, Almazov AA. Optimization of multi-tip field emission electron source. Vacuum 1999; 52(3) 295-300.

[28] Xu N, Wu Z, Deng S, et al. High-voltage triode flat-panel display using field-emission nanotube-based thin films. Journal of Vacuum Science & Technology B: Microelectronics and Nanometer Structures 2001; 19(4) 1370-1372.

[29] Jung J, Jin Y, Choi J, Park Y, Ko T, Chung D, Kim J, Jang J, Cha S, Yi W. Fabrication of triode-type field emission displays with high-density carbon-nanotube emitter arrays. Physica B: Condensed Matter 2002; 323(1-4) 71-77.

[30] Kim K, Song Y, Hwang C, et al. Efficient electron emissions from printed carbon nanotubes by surface treatments. Journal of Vacuum Science & Technology B: Microelectronics and Nanometer Structures 2004; 22(3) 1331-1334.

[31] Choi Y, Kang J, Kim H, et al. A simple structure and fabrication of carbon-nanotube field emission display. Applied Surface Science 2004; 221(1-4) 370-374.

[32] Nishimura K, Shen Z, Fujikawa M, et al. Fabrication of carbon-nanotube field-emitter array using polymer insulator. Journal of Vacuum Science & Technology B: Microelectronics and Nanometer Structures 2004; 22(3) 1377-1381.

[33] Kim H, et al. Fabrication of field emission triode using carbon nanotubes. Materials Science and Engineering: C 2001; 16(1-2) 27-30.

[34] Shiratori Y, Hiraoka H, Takeuchi Y, et al. One-step formation of aligned carbon nanotube field emitters at 400 °C. Applied Physics Letters 2003; 82(15) 2485-2487.

[35] Jang Y, Choi C, Ju B, et al. Fabrication and characteristics of field emitter using carbon nanotubes directly grown by thermal chemical vapor deposition. Thin Solid Films 2003; 436(2) 298-302.

[36] Chuang CC, Huang JH, Lee CC, Chang YY. Fabrication and field emission characteristics of high density carbon nanotube microarrays. Journal of Vacuum Science & Technology B: Microelectronics and Nanometer Structures 2005; 23(2) 772-775.

[37] Shulitski BG, Labunov VA, Prudnikava EL. Investigation of the multi-wall carbon nanotube synthesis process with the regulated parameters. In: Krokhin ON (ed.) International Symposium "Advanced Display Technologies": Symposium Proceedings of the 15th International Symposium "Advanced Display Technologies", 3-5 October 2006, Moscow, Russia. p63-61.

[38] Vorobyova AI, Shulitski BG, Prudnikava EL. Formation of anodic aluminum oxide matrix for carbon nanotube growth. Nano- and Microsystems Engineering 2007;86(7) 39-43 (in Russian).

[39] Jeong SH, Lee KH. Fabrication of the aligned and patterned carbon nanotube field emitters using the anodic aluminum oxide nano-template on a Si wafer. Synthetic Metals 2003; 139(2) 385-390.

[40] Davydov D, Sattari P, Almawlawi D, Osika A, Haslett T, Moskovits M. Field emitters based on porous aluminum oxide templates. Journal of Applied Physics 1999; 86 3983.

[41] Hu W, Yuan L, Chen Z, Gong D, Saito K. Fabrication and characterization of vertically aligned carbon nanotubes on silicon substrates using porous alumina nanotemplates. Journal of Nanoscience and Nanotechnology 2002; 2(2) 203-207.

[42] Gao H, Mu C, Wang F, Xu D, Wu K, Xie Y, Liu S, Wang E, Xu J, Yu D. Field emission of large-area and graphitized carbon nanotube array on anodic aluminum oxide template. Journal of Applied Physics 2003; 93 5602.

[43] Yu W, Cho YS, Choi GS, Kim D. Patterned carbon nanotube field emitter using the regular array of an anodic aluminium oxide template. Nanotechnology 2005; 16 S291.

[44] Cho YS, Song IK, Hong SK, Im WS, Choi GS, Kim D. Synthesis mechanism of flaked carbon nanotubes formed on an anodic aluminum oxide template examined via transmission electron microscopy. Journal of the Korean Physical Society 2005; 47(2) 344-347.

[45] Im WS, Cho YS, Choi GS, et al. Stepped carbon nanotubes synthesized in anodic aluminum oxide templates. Diamond and Related Materials 2004; 13(4-8) 1214-1217.

[46] FUG ElektronikGmbH, http://www.fug-elektronik.de.

[47] Keithley Instruments GmbH, http://www.keithley.de.

[48] Navitski A. Scanning field emission investigations of structured CNT and MNW cathodes, niobium surfaces and photocathodes. PhD thesis. Univ. of Wuppertal; 2010.

[49] Lysenkov D, Müller G. Field emission measurement techniques for the optimisation of carbon nanotube cathodes. International Journal of Nanotechnology 2005; 2(3) 239-254.

[50] Forbes RG. Field emission: New theory for the derivation of emission area from a Fowler-Nordheim plot. Journal of Vacuum Science & Technology B: Microelectronics and Nanometer Structures 1999; 17 526.

[51] Navitski A, Müller G, Sakharuk V, Cornelius T, Trautmann C, Karim S. Efficient field emission from structured gold nanowire cathodes. The European Physical Journal Applied Physics 2009; 48(03) 30502.

[52] Bonard JM, Dean KA, Coll BF, Klinke C. Field emission of individual carbon nanotubes in the scanning electron microscope. Physical Review Letters 2002; 89(19) 197602.

[53] Zhong D, Zhang G, Liu S, Sakurai T, Wang E. Universal field-emission model for carbon nanotubes on a metal tip. Applied Physics Letters 2002; 80 506.

[54] Dangwal A, Pandey C, Müller G, Karim S, Cornelius T, Trautmann C. Field emission properties of electrochemically deposited gold nanowires. Applied Physics Letters 2008; 92 063115.

[55] Nikon Corporation, http://www.nikon.com/.

[56] Basler AG, http://www.baslerweb.com.

[57] Matrox Meteor II, Matrox Electronic Systems GmbH, http://www.matrox.com.

[58] Olympus Soft Imaging Solutions GmbH, www.olympus-sis.com.

[59] Dangwal A, Reschke D, Müller G. DC field emission scanning measurements on electropolished niobium samples. Physica C: Superconductivity 2006; 441(1) 83-88.

[60] Labunov V, Shulitski B, Prudnikava A, Shaman J, Smirnov A, Navitski A, Müller G. CNT Field Emission Cathodes for Micro FEDs. In: Proceedings of the 14th International Display Workshops: IDW'07, 5-7 December 2007, Sapporo, Japan, 2007, 3. p2181-2184.

[61] Labunov VA, Shulitski BG, Prudnikava EL, Navitski A, Basaev A, Müller G, Priyatkin N. Field Emission Cathodes based on meander-shape arrays of vertically aligned carbon nanotubes. Nano- and Microsystems Engineering 2009; 113(12) 30-38 (in Russian).

[62] Equipment for carbon nanostructures synthesis: Eurasian Patent., B82B 3/00 (2006.01), D01F 9/133 (2006.01) / Saurov A, Basaev A, Labunov V, Shulitski B, Pavlov A, Prudnikava A, Shaman Y, Galperin V; declarant: Federal State Founding "Scientific Production Cpmplex "Technological Center" of the Moscow State Institute of Electronic Engineering", № 015412 ; published 30.08.11 // Official bulletin / Eurasian Patent Office, 2011.

[63] Shulitski B, Labunov V, Prudnikava A, Balk L, Heiderhoff R. Selective growth of carbon nanotube arrays synthesized by injection CVD method. In: Borisenko VE (ed.) Physics, chemistry and application of nanostructures: reviews and short notes: proceedings of the international conference, Nanomeeting-2007, 22-25 May 2007, Minsk, Belarus, Singapore: World Scientific Pub Co Inc. p458-462.

[64] Prudnikava A. Formation of ordered carbon nanotube arrays, composite nanostructures based on them by the injection chemical vapour deposition. PhD thesis (in Russian), Belarusian State University of Informatics and Radioelectronics; 2011.

[65] Labunov VA, B. G. Shulitski, E. L. Prudnikava, Yanushkevitch KI. Structure, composition and magnetic properties of carbon nanotubes doped by Fe during the growth process. Journal of Physics: Conference Series 2008; 100(5) 052095.

[66] Basaev A, Bokhonov B, Demidenko O, Labunov V, Makovetskii G, Prudnikova E, Reznev A, Saurov A, Fedosyuk V, Fedotova YA. Synthesis and properties of magnetically functionalized carbon nanotubes. Nanotechnologies in Russia 2008; 3(3) 184-190.

[67] Labunov V, Prudnikava A, Yanushkevich K, Basaev A, Danilyuk A, Fedotova Y, Shulitskii B. Synthesis and Properties of the Arrays of Magnetically Functionalized Carbon Nanotubes. In: Marulanda J (Eds.) Carbon Nanotubes Applications on Electron Devices, Rijeka: InTech; 2011.

[68] Lysenkov D, Müller G. Improved current densities of carbon nanotube cathodes by pulsed operation. Improved current densities of carbon nanotube cathodes by pulsed operation. Journal of Vacuum Science & Technology B: Microelectronics and Nanometer Structures 2006; 24(2) 1067-1071.

[69] http://www.videotest.ru St.-Petersburg, Russia

[70] Ding F, Bolton K, Rosen A, Molecular dynamics study of bamboo-like carbon nanotube nucleation. Journal of Electronic Materials 2006; 35(2) 207-210.

[71] Dean KA, Burgin TP, Chalamala BR. Evaporation of carbon nanotubes during electron field emission. Applied Physics Letters 2001; 79(12) 1873-1875.

[72] Semet V, Binh VT, Vincent P, Guillot D, Teo K, Chhowalla M, Amaratunga GAJ, Milne W, Legagneux P, Pribat D. Field electron emission from individual carbon nanotubes of a vertically aligned array. Applied Physics Letters 2002; 81 343.

[73] Nilsson L, Groening O, Emmenegger C, Kuettel O, Schaller E, Schlapbach L, Kind H, Bonard J, Kern K. Scanning field emission from patterned carbon nanotube films. Applied Physics Letters 2000; 76 2071.

[74] Fan S, Chapline MG, Franklin NR, Tombler TW, Cassell AM, Dai H. Self-oriented regular arrays of carbon nanotubes and their field emission properties. Science 1999; 283(5401) 512-514.

[75] Teo K, Chhowalla M, Amaratunga G, Milne W, Hasko D, Pirio G, Legagneux P, Wyczisk F, Pribat D, Uniform patterned growth of carbon nanotubes without surface carbon. Applied Physics Letters 2001; 79 1534.

[76] Lysenkov D, Engstler J, Dangwal A, Popp A, Müller G, Schneider JJ, Janardhanan VM, Deutschmann O, Strauch P, Ebert V. Nonaligned Carbon Nanotubes Anchored on Porous Alumina: Formation, Process Modeling, Gas-Phase Analysis, and Field-Emission Properties. Small 2007; 3(6) 974-985.

[77] Labunov VA, Shulitski BG, Prudnikava AL, Shaman YP, Basaev AS. The effect of gas-dynamic factors on selective carbon-nanotube synthesis by injection CVD method for field-emission cathodes. Journal of the Society for Information Display 2009; 17(5) 489-495.

[78] Navitski A, Müller G, Sakharuk V, Prudnikava AL, Shulitski BG, Labunov VA. Efficient high-current field emission from arrays of carbon nanotube columns. Journal of Vacuum Science & Technology B: Microelectronics and Nanometer Structures 2010; 28(2) C2B14-C2B19.

[79] Gröning O, Nilsson L, Gröning P, Schlapbach L. Properties and characterization of chemical vapor deposition diamond field emitters. Solid-State Electronics 2001; 45(6) 929-944.

[80] Chen X, Chang Y, Wang Z, Yu D. Effect of ion beam etching on the field emission of carbon nanotube arrays. Solid state communications 2009; 149(13-14) 523-526.

[81] Kwon SJ. Effects on Field Emission Characteristics of Ar Ion Bombardment for Screen-Printed Carbon Nanotube Emitters. Japanese Journal of Applied Physics 2007; 46 5988.

[82] Bormashov VS, Baturin AS, Nikolskiy KN, Tschesov RG, Sheshin EP. The current stability of field emission cathodes of carbon nanotubes under ion bombardment. Surface and Interface Analysis 2007; 39(2-3) 155-158.

[83] Saeidi Mohammadreza, Majid Vaezzadeh. Ultra-long carbon nanotube growth on catalyst. Physica E: Low-dimensional Systems and Nanostructures 2009; 41(9) 1723-1726.

[84] Chen PL, Chang JK, Kuo CT, Pan FM. Anodic aluminum oxide template assisted growth of vertically aligned carbon nanotube arrays by ECR-CVD. Diamond and Related Materials 2004; 13(11-12) 1949-1953.

[85] Jung M, Kim HG, Lee JK, Joo OS, Mho S. EDLC characteristics of CNTs grown on nanoporous alumina templates. Electrochimica Acta 2004; 50(2-3) 857-862.

[86] Kim MJ, Lee TY, Choi JH, Park JB, Lee JS, Kim SK, Yoo JB, Park CY. Growth of carbon nanotubes with anodic aluminum oxide formed on the catalytic metal-coated Si substrate. Diamond and Related Materials 2003; 12(3-7) 870-873.

[87] Gorokh G. High-ordered anodic alumina films for nanostructure forming. In: Yakovleva N. (ed.) Proceedings of School-Seminar «Nanostructured oxide films and coating», 24 – 27 October 2007, Petrozavodsk, Republic of Karelia. p62-68 (in Russian).

[88] Solovei D, Sakharuk V, Mozalev A, Navitski A, Prudnikava A, Gorokh G, Mueller G. Influence of various contact interfaces between carbon nanotubes and porous-alumina-coated n-type Si wafers on field emission properties. In: Extended abstracts of 21th International Vacuum Nanoelectronics Conference (IVNC), 13-17 July, 2008, Wrocław, Poland.

[89] Solovei D, Sakharuk V, Gorokh G. Field emission behavior of carbon nanotubes embedded into anodic alumina pores on metal oxide catalysts. Doklady BGUIR 2008; 5(35) 42-49 (in Russian).

[90] Gorokh G, Solovei D, Mozalev A. Features of formation of anodic alumina films on n-Si wafers. In: Yakovleva N. (ed.) Proceedings of School-Seminar «Nanostructured oxide films and coating», 24-27 October 2007, Petrozavodsk, Republic of Karelia. p18 (in Russian).

[91] Gorokh G, Mozalev A, Solovei D, Sakharuk V. Synthesis of Nickel Nanowires in Anodic Alumina Pores. In: Proceedings of the 16th International Conference «Microwave & Telecommunication Technology» (CriMiCo 2006), 11-15 September 2006, Sevastopol, Crimea, Ukraine. p673-674 (in Russian).

[92] Solovei D, Mozalev A, Gorokh G. Formation of highly ordered anodic alumina matrixes given thickness and morphology. Doklady BGUIR 2008; 6(36) 65-73 (in Russian).

[93] Solovei D, Sakharuk V, Gorokh G. Arrays of nickel field nanocathodes based on anodic alumina matrixes. Proceedings of the National Academy of Sciences of Belarus. Physico-technical series 2011; 1 90-96 (in Russian).

[94] Gorokh G, Mozalev A, Solovei D, Shulitski B, Labunov V. Synthesis of ordered carbon nanotubes arrays on nickel catalysts in anodic alumina pores. In: Proceedings of the II Russian Conference on Nanomaterials, NANO-2007, 13-16 March, 2007, Novosibirsk, Russia. p132 (in Russian).

[95] Solovey D, Prudnikava A, Gorokh G. Influence of contact interfaces between carbon nanotubes and Si substrate on the field emission properties of nanostructures. Proceedings of the National Academy of Sciences of Belarus. Physics and Mathematics Series 2009; 1 114-119 (in Russian).

[96] Solovey D, Sakharuk V, Gorokh G. Study of Field Emission Characteristics of nickel nanocathodes arrays in anodic alumina

matrix. Vacuum technique and technology 2010; 20(2) 95-100 (in Russian).

[97] Gorokh G, Solovey D, Sakharuk V. Field emission behaviour of carbon nanotubes embedded into anodic alumina pores on metal oxide catalists. In: Proceedings of the 18th International Conference «Microwave & Telecommunication Technology» (CriMiCo 2008), 10-14 September 2008, Sevastopol, Crimea, Ukraine. p616-618 (in Russian).

[98] Valentini L, Lozzi L, Cantalini C, Armentano I, Kenny JM, Ottaviano L, Santucci S. Effects of oxygen annealing on gas sensing properties of carbon nanotube thin films. Thin Solid Films 2003; 436(1) 95-100.

[99] Dillon AC, Mahan AH, Alleman JL, Heben MJ, Parilla PA, Jones KM. Hot-wire chemical vapor deposition of carbon nanotubes. Thin Solid Films 2003; 430(1-2) 292-295.

[100] Mercier S, Ehrburger P, Lahaye J. Interfacial reactivity in aluminium/carbon fibre composites. Journal de Physique IV France 1993; 03(C7) C7-1723-C7-1726.

[101] Labunov V, Prudnikava A, Solovei D, Gorokh G, Shulitski B, Sakharuk V, Navitski A, Müller G, Basaev A. Structured Carbon Nanotubes Based Field Emission Cathodes. In: Proceedings of the 29th International Display Research Conference (Eurodisplay 2009), 14-17 September 2009, Rome, Italy. p248-250.

[102] Solovei D, Sakharuk V, Navitski A, Gorokh G, Müller G. Matrixes of field emission cathodes based on carbon nanotubes in porous anodic alumina. In: Proceedings of the 19th International Conference «Microwave & Telecommunication Technology» (CriMiCo 2009), 14-18 September 2009, Sevastopol, Crimea, Ukraine. p601-604 (in Russian).